

# **Understanding role of point defects on electronic properties in 2D materials**

Dual Degree Thesis Report

*Submitted in fulfilment of the requirements for the degree of Bachelor of Technology & Master of Technology*

By

**Shashank Raut Desai**

(Roll No. 17D110006)

Supervisor:

**Prof. Sumit Saxena**



Department of Metallurgical Engineering and Materials Science

INDIAN INSTITUTE OF TECHNOLOGY BOMBAY

(October 2021)

## **Declaration**

I declare that this written submission represents my ideas in my own words and where others ideas or words have been included; I have adequately cited and referenced the original source. I also declare that I have adhered to all principles of academic honesty and integrity and have not misrepresented or fabricated or falsified any idea/data/fact/ source in my submission. I understand that any violation of the above will be cause for disciplinary action by the institute and can evoke penal action from the sources, which have thus not been properly cited, or from whom the proper submission has not been taken when needed.

---

**Shashank Raut Desai**

**17d110006**

## Approval Sheet

Dissertation titled 'Understanding role of point defects on electronic properties in 2D materials' by Mr. Shashank Raut Desai is approved for the Dual Degree (Bachelor of Technology & Master of Technology) in Metallurgical Engineering and Materials Science (MEMS) at IIT Bombay.

**Examiner(s):**

---

**Supervisor:**

---

**Chairman:**

---

**Date:** \_\_\_\_\_

**Place:** \_\_\_\_\_

## Acknowledgement

I would like to express my heartfelt thanks and sincere respect for my guide, Prof. Sumit Saxena, for sharing his immense knowledge with me and empowering me with the art and science of research. His constant motivation and capable counsel inspired me, instilling me with a sense of self-assurance. I also want to thank the Metallurgical Engineering and Material Science Department, Indian Institute of Technology, Bombay for giving me the opportunity and resources to work on this riveting topic.

I am deeply grateful to Dr. Basant Roondhe for easing me into the world of molecular simulations and helping me in getting comfortable with simulation software. His consistent encouragement has shaped my interest in this field.

Finally, I would like to thank my family for their endless support and countless sacrifices, for which I am eternally obliged.

# Abstract

Ever since Novoselov and Geim successfully isolated the single-layer graphene in 2004 and published their paper, the field of two-dimensional materials has seen a renaissance of interest by research groups all over the world after a few decades, with their paper in the Science journal becoming one of the hundred most cited papers of all time. The outstanding properties exhibited by graphene and the ensuing masses of 2D materials synthesized thereafter, have proven to be useful for an endless set of applications. In this report, we examine what constitutes a 2D material, their general electrical, mechanical and optical properties and some popular classes of 2D materials.

Further, we study molybdenum disulphide, one of the most researched 2D materials, and its properties along with some of its applications in the fields of electronics, medicine and energy. Next, the types of defects that exist in 2D materials are studied, with special emphasis on the defects found in molybdenum disulphide. We proceed to conduct computational studies on vacancy defects found in MoS<sub>2</sub> using Quantum Espresso to perform ab initio electronic structure calculations and present our results, along with laying the path for future work.

## List of Figures

Figure 1: Examples of different types of structures, classified by dimensions [3] (Creative Commons License) .....	8
Figure 2: Representative Diagram of Mechanical Exfoliation [15] (Creative Commons License) ..	13
Figure 3: Representative Diagram of Chemical Exfoliation [15] (Creative Commons License) .....	14
Figure 4: Band structure of graphene [19] (Creative Commons License) .....	15
Figure 5: Graphene monolayer [21] (Creative Commons License) .....	16
Figure 6: Two-dimensional structure of WTe <sub>2</sub> [25] (Creative Commons License) .....	17
Figure 7: Buckled hexagonal structure of stanene and silicene, respectively [27] (Creative Commons License) .....	18
Figure 8: Types of monolayer MoS <sub>2</sub> : 1T (left), 2H (right) [31] (Creative Commons License) .....	19
Figure 9: Effect of various agents on cancer cells in mice [37] (Creative Commons License) .....	22
Figure 10: 1. Block diagram of conventional imaging system, 2. Neuromorphic imaging device [40] (Creative Commons License).....	22
Figure 11: Reconstructed vacancy in graphene with atomic configuration - 9 and 5 membered ring [46] (Creative Commons License).....	25
Figure 12: SW defect in graphene [46] (Creative Commons License).....	25
Figure 13: (1,1) Line defect in graphene [22] (Creative Commons License) .....	26
Figure 14: Grain boundary defect [22] (Creative Commons License) .....	27
Figure 15: Sulphur monovacancy V <sub>S</sub> point defect [48] (Creative Commons License) .....	28
Figure 16: Vacancy complex V <sub>MoS3</sub> [48] .....	28
Figure 17: 5 7 dislocation in MoS <sub>2</sub> [48] (Creative Commons License).....	29
Figure 18: 4 6 dislocation in MoS <sub>2</sub> [48] (Creative Commons License).....	29
Figure 19: 4 4P 60° grain boundary structure [48] (Creative Commons License) .....	30
Figure 20: Flowchart of self-consistent Kohn-Sham calculation [54].....	35
Figure 21: Flowchart of unit cell optimization.....	37
Figure 22: Optimization of Kinetic Energy Cutoff.....	39
Figure 23: Optimization of Monkhorst-Pack Grid .....	40
Figure 24: Unit cell definition using parallelopiped with lengths $a$ , $b$ , $c$ and angles between the sides given by $\alpha$ , $\beta$ , $\gamma$ .....	40
Figure 25: Optimization of Lattice Parameter.....	41
Figure 26: Side view of 1x1x1 MoS <sub>2</sub> unit cell, visualized in Xcrysden .....	41
Figure 27: Top view of 1x1x1 MoS <sub>2</sub> unit cell, visualized in Xcrysden .....	42

Figure 28: K-Path Selection .....	43
Figure 29: Band structure of pristine monolayer MoS <sub>2</sub> .....	43
Figure 30: Density of states for pristine monolayer MoS <sub>2</sub> unit cell .....	44
Figure 31: Projected Density of states for monolayer MoS <sub>2</sub> unit cell .....	44
Figure 32: Simulated STM image of unit cell .....	45
Figure 33: Top view of 3x3x1 MoS <sub>2</sub> supercell, visualized in Xcrysden.....	46
Figure 34: Side view of 3x3x1 MoS <sub>2</sub> supercell, visualized in Xcrysden .....	46
Figure 35: Band structure of 3x3x1 MoS <sub>2</sub> supercell .....	47
Figure 36: Density of states for pristine 3x3x1 super cell.....	47
Figure 37: Projected Density of states for super cell .....	48
Figure 38: Simulated STM image of super cell.....	48
Figure 39: Top view of MoS <sub>2</sub> supercell molecular structure with V <sub>s</sub> defect .....	49
Figure 40: Side view of MoS <sub>2</sub> supercell molecular structure with V <sub>s</sub> defect.....	49
Figure 41: Band structure of MoS <sub>2</sub> with V <sub>s</sub> defect .....	50
Figure 42: Density of states plot of MoS <sub>2</sub> with V <sub>s</sub> defect .....	51
Figure 43: Projected Density of states plot of MoS <sub>2</sub> with V <sub>s</sub> defect.....	51
Figure 44: Simulated STM image of MoS <sub>2</sub> with V <sub>s</sub> defect.....	52
Figure 45: Top view of MoS <sub>2</sub> supercell molecular structure with V <sub>Mo</sub> defect.....	52
Figure 46: Side view of MoS <sub>2</sub> supercell molecular structure with V <sub>Mo</sub> defect.....	53
Figure 47: Band structure of MoS <sub>2</sub> with V <sub>Mo</sub> defect.....	53
Figure 48: Density of states plot of MoS <sub>2</sub> with V <sub>Mo</sub> defect .....	54
Figure 49: Density of states plot of MoS <sub>2</sub> with V <sub>Mo</sub> defect .....	54
Figure 50: Simulated STM image of MoS <sub>2</sub> with V <sub>Mo</sub> defect.....	55

# Table of Contents

1. Introduction.....	8
1.1 Zero Dimensional Nanostructured Materials .....	9
1.2 One Dimensional Nanostructured Materials .....	9
1.3 Two Dimensional Nanostructured Materials .....	9
1.4 Three Dimensional Nanostructured Materials .....	10
2. Two Dimensional Materials .....	11
2.1 Properties of 2D.....	11
2.1.1 Electrical Properties .....	11
2.1.2 Optical properties of 2D materials .....	12
2.1.3 Mechanical properties of 2D materials .....	12
2.2 Methods of Synthesis.....	13
2.2.1 Top Down Approach.....	13
2.2.2 Bottom-up approach.....	14
2.3 Some important types of two-dimensional materials .....	15
2.3.1 Graphene.....	15
2.3.2 Two Dimensional Transitional Metal Dichalcogenides .....	16
2.3.3 Xenos .....	17
3. Molybdenum disulphide .....	19
3.1 Introduction .....	19
3.2 Properties .....	19
3.3 Applications of MoS <sub>2</sub> .....	21
3.3.1 Medical Applications .....	21
3.3.2 Electronic Applications .....	22
3.3.3 Energy Applications .....	23
4. Point Defects.....	24
4.1 Introduction to defects in 2D materials.....	24
4.2 Types of defects in 2D materials .....	24
4.2.1 Zero Dimensional.....	24
4.2.2 One Dimensional.....	26
4.3 Defects observed in MoS <sub>2</sub> .....	27
4.3.1 Point Defects.....	27



4.3.1 Dislocations and GBs .....	28
4.4 Why study point defects?.....	30
5. Density Functional Theorem .....	31
5.1 Need for Computational Studies .....	31
5.2 Origin of Computational Studies.....	31
5.3 Many Body Problem.....	32
5.4 Wave Function Based Method To Solve Many-Body Equation.....	33
5.4.1 Hohenberg-Kohn Theory.....	33
6. Results .....	37
6.1 Background .....	37
6.2 Computation Process .....	37
7. Summary & Future work.....	56
7.1 Summary .....	56
7.2 Future Work .....	56
8. References .....	57

# 1. Introduction

The 21<sup>st</sup> century has seen a rapid increase in the pace of development in technology. For this development, a dominant aspect to study is the material system behind the technology. Here, material system refers to the characteristics of the material, behaviour of the material and the like. Each material has its own distinct set of properties which can be used for different types of applications. [1]

The size of material is a key factor in determining the characteristics of a material. This is because the nature of the material itself varies with the size at which we observe the properties of the material. At the nanoscale size, the behaviour as well as the chemical, mechanical and electrical characteristics of the material vary tremendously. Materials with at least one dimension in the range of 1nm to 100nm are classified as nanomaterials. Pokropivny and Skorokhod [2] proposed a classification scheme for nanomaterials under which they can be divided into four types of materials: zero-dimensional, one-dimensional, two-dimensional and three-dimensional. Depending on their properties, materials may

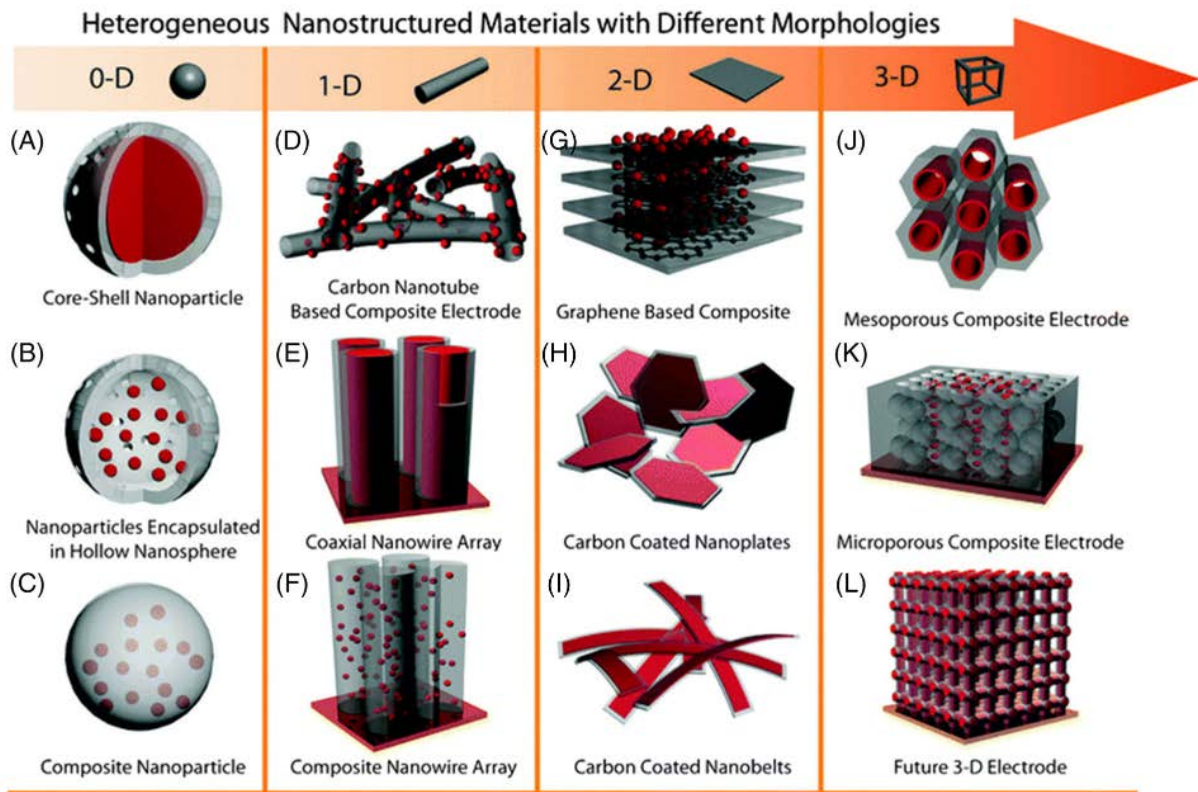


Figure 1: Examples of different types of structures, classified by dimensions [3] (Creative Commons License)

vary by shape, by their atomic structure and even by states to be in the bulk form, solution form or liquid form.

### **1.1 Zero Dimensional Nanostructured Materials**

If all of the three dimension of a material are nanosized, that is, in the range of 1nm to 100nm, then the material is a 0D NSM (nanostructured materials). [1] Several physical and chemical techniques of fabrication of 0D nanomaterials have evolved. Multiple research groups have managed to synthesize quantum dots (homogeneous particle arrays), heterogeneous particles arrays, core shell quantum dots, onions, hollow spheres and nanolenses. [3]

### **1.2 One Dimensional Nanostructured Materials**

When two dimensions of a material are nanosized, that is, in the range of 1nm to 100nm, and one dimension is in the range of 1mm to 10cm, then the material is a 1D NSM. [1] 1D NSMs have generated a lot of interest and have a variety of potential applications. Conventionally, 1D NSMs are ideal to study several novel phenomena at nanoscale as well as relation of material behaviour with size and dimensionality. Some examples of 1D NSMs are nanorods (solid nanofiber), nanowires (electrically conducting/semi-conducting nanofiber), nanobelts, nanotubes (hollow nanofiber), hierarchical nanostructures and nanoribbons. In the future, 1D NSMs are anticipated to be vital as the interconnects as well as the main component in producing electronic and optoelectronic nanodevices. [3]

### **1.3 Two Dimensional Nanostructured Materials**

When only one of the three dimensions of a material is in the range of 1nm to 100nm and the other two dimensions are larger than nanoscale size, then the material is considered a 2D nanostructured material. [1] Some examples include nanosheet, nanowall, nanodisk, nanoprism and so on. With certain geometry, they show characteristic characteristics which vary with shape and hence, they can be used as building block of important constituents of nanodevices. 2D materials can also be used for

fabricating devices like sensors, transistors, photodetectors, battery electrodes, photocatalyst, nanoreactors and templates for 2D structures of other NSMs. [3]

#### **1.4 Three Dimensional Nanostructured Materials**

When all the three dimensions of a material are greater than nanosize (range of 1nm to 100nm) that is, micro or larger in size, then the material is considered a 3D nanostructured material. [1] Some examples of 3D NSMs include nanopillars, nanoballs, nanoflowers nanocoils and nanocones. Due to their larger surface and sufficient sites of absorption in a limited space, they have garnered significant interest. Substances with porousness in all the 3 dimensions may give rise to better molecular transport. [3]

In our paper, we'll focus on studying two-dimensional materials and the unique properties they exhibit rising from point defects in their structure.

## 2. Two Dimensional Materials

Ever since Novoselov and Geim [4] were able to successfully isolate the single layer graphene, there has been explosive interest in the field of two-dimensional materials. Two-dimensional materials offer unique possibilities to study previously uncharted areas of materials science. The ultra low thickness that 2D materials provide, make them suitable for use in electronics like FETs (field effect transistors) in which a small size of equipment enhances performance of the device as well as cuts down on the short-channel effects between the contacts. [5] MLs (monolayers) vary significantly in their physical properties from the parent three-dimensional materials as MLs furnish an extra DOF (degree of freedom) for various applications and give rise to phenomena like composite excitations (trions) and valley Hall effect. Additionally, van der Waals heterostructures rose up as an area to fabricate unique phenomena by stacking layers of two dimensional materials as required. [6]

### 2.1 Properties of 2D

#### 2.1.1 Electrical Properties

In two-dimensional semi-conductors, electrical properties are conventionally confirmed by the exhibition of the field effect in FETs. A lot of research has been done to improve FET devices viz a viz their performance, with special interest in optimising the device junction. According to Lim and his team, a unique FET comprising a 2D MoS<sub>2</sub>-black phosphorus hetero-junction would show exceptionally low sub-threshold swing (54mV/dec) high ON/OFF ratio greater than 10<sup>7</sup> and low off current at 1 A. [7] The small value of off current is due to the presence of a depletion region in black phosphorus. The FET properties of a device can be improved by inserting a TiO<sub>2</sub> interfacial layer between 2D transition metal dichalcogenide (TMDC) like WSe<sub>2</sub> and metal. [8] Electrical properties can be stabilized under gate bias stress condition because the interfacial layer will perform Fermi level depinning, hence reducing density of interface states. [9] The preparation of p type MoS<sub>2</sub> is generally required for the complementary integration of n and p type 2D materials. Adding a dopant precursor of P<sub>2</sub>O<sub>5</sub> during production of MoS<sub>2</sub> via CVD can yield p type semiconducting properties, according to Lee et al. [10] When compared to undoped n-type MoS<sub>2</sub>, the p-type doped monolayer MoS<sub>2</sub> demonstrated p-type conduction with field effect mobility of 0.023 cm<sup>2</sup>/Vs an ON-OFF ratio of 10<sup>3</sup>. The p-doped FET's performance should be improved even further. Recently, in the development of a neuromorphic hardware system, artificial synapse devices have become regarded as one of the most important components. It's very important to seek a physical parameter that

properly regulates synaptic plasticity. [9] In a paper by Kim et al, a 2D FET with Nb<sub>2</sub>O<sub>5</sub>/ WSe<sub>2</sub>/NbSe<sub>2</sub> heterostructure which utilized thickness of Nb<sub>2</sub>O<sub>5</sub> layer to regulate the post synaptic current, hence regulating synaptic plasticity. [11]

### 2.1.2 Optical properties of 2D materials

2D materials often exhibit novel optical properties, which have been researched by several groups. [9] Utilizing ultrathin AFM tips, reversibly controllable photoluminescence was achieved during ferroelectric polarisation reversal using thin semiconductor MoS<sub>2</sub>/ferroelectric lead zirconium titanate heterostructure sheets. [12] The spontaneous polarisation of ferroelectric thin films impacts the opto electronic properties of MoS<sub>2</sub>.

Raman spectra of black phosphorus deposited on a Ge-coated dimethicone substrate was investigated, and distinct peak shifting rates for the Ag<sup>1</sup>, B<sub>2g</sub>, and Ag<sup>2</sup> modes were observed for various BP layer thicknesses. [13] The observation of the strain–Raman spectrum relationship revealed a maximum uniaxial strain of 0.89 percent. This shifting phenomena was accurately recorded. According to research on PL and Raman spectrum undertaken by Zhang et al, bilayer MoS<sub>2</sub> was benchmarked with ML MoS<sub>2</sub>. Doping along with substrate-film strain cause interlayer difference. PL and Raman spectroscopy can identify surface variations with thickness of less than mono-atom layer, thus generating insightful data regarding the impact of 2D vdW (van der Waals) homo and hetero structures on its optical properties. [9]

### 2.1.3 Mechanical properties of 2D materials

Several 2D materials have gathered a lot of interest for their unique mechanical properties. Two-dimensional materials have high elastic modulus, extremely low weight, excellent carrier mobility, high strength and high anisotropy in out-of-plane and in-plane mechanical properties. Covalent bonding attaches neighbouring atoms in the same plane, whereas weak vdW forces hold together the interlayers. [14] These weak vdW forces enable layers to slide over each other when stress coplanar with surface area is applied, hence causing lubrication. Adding WS<sub>2</sub> nanoflowers in paraffin oil can improve abrasion and wear protection. This is because of nanoflowers' morphology, which leads to formation of a uniform tribofilm during the sliding motion. [9]

## 2.2 Methods of Synthesis

Since some materials have 3D molecular linkages, thinning the substance necessitates breaking these links, leaving behind hanging bonds. Such a 2D material would have dangling bonds which are highly chemically and thermodynamically unstable, leading it to rearrange its shape in order to minimise its surface energy. A graphite allotrope contains solid chemical linkage along the planes in bulk material.

These layers are piled together and kept together by a weak vdW force, but can be separated with no loose bonds. The methods of synthesizing two dimensional materials can be classified in two categories: top down and bottom up. [1]

### 2.2.1 Top Down Approach

#### 2.2.1.1 Mechanical Exfoliation

Novoselov and Geim used mechanical exfoliation to synthesize graphene in 2004. In this method, a piece of adhesive tape is placed on the stacked material's surface and peeled away, leaving flakes behind. The flakes can be deposited on the substrate by pressing Scotch tape against it. This process produces a limited yield of MLs, with no modulation of size or shape. The ML produced has few defects and sufficient size in the range of 1-100 $\mu\text{m}$ . This is not suitable for large scale manufacturing. [1]

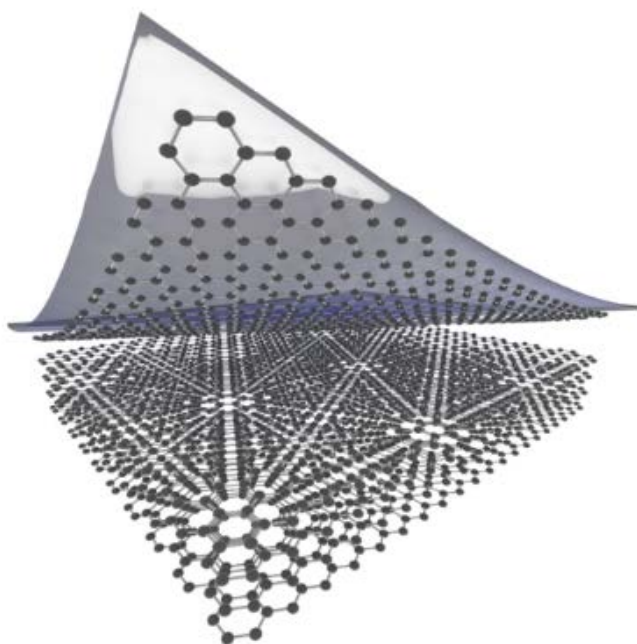


Figure 2: Representative Diagram of Mechanical Exfoliation [15] (Creative Commons License)

### 2.2.1.2 Liquid Exfoliation

An organic solvent is employed as a medium to apply mechanical force to the substance (generally a powder suspended in liquid). By transferring tensile stress to layers of material, sonication causes them to split. Reactive ions are added (which form hydrogen bubbles between planes) to push layers apart or solution is rapidly mixed to increase shear force to enhance ML yield. This method produces low yield of MLs with smaller flakes lesser than 100nm in size. These flakes have high concentration of defects along with residual solvent. [1]

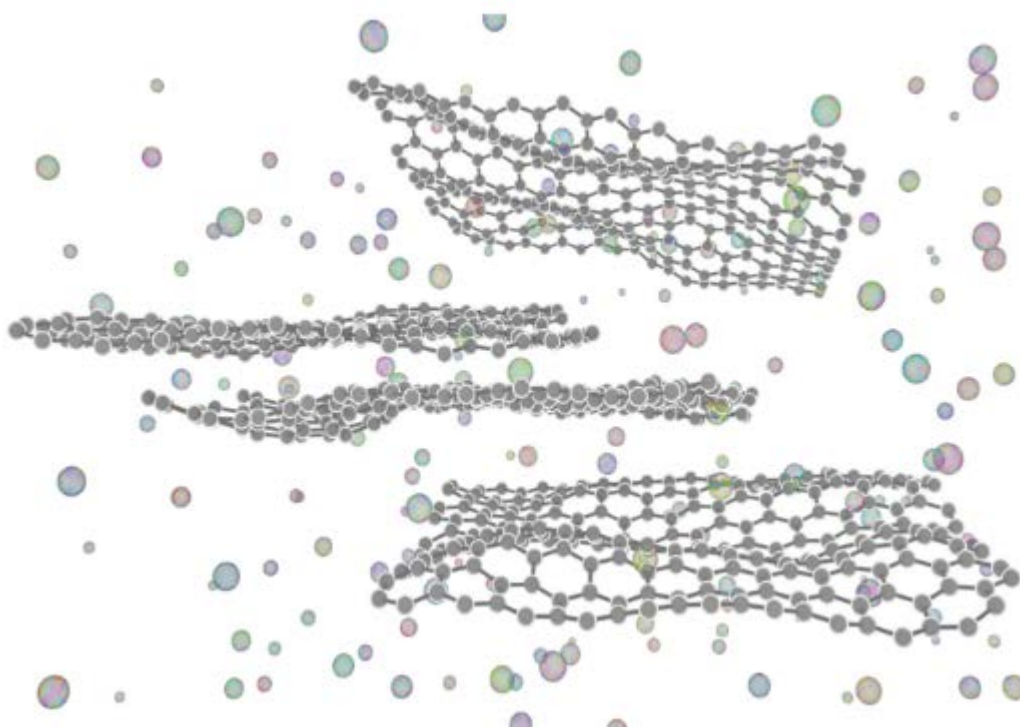


Figure 3: Representative Diagram of Chemical Exfoliation [15] (Creative Commons License)

### 2.2.2 Bottom-up approach

#### 2.2.2.1 Chemical synthesis in solution

Some wet chemical methods of chemical synthesis of 2D materials include: reactions in solutions under high temperature, amalgamation of nanoparticles into nanosheets, interface-controlled growth and so on. These can be used to synthesize most types of 2D materials. This method also produces low yield of MLs with smaller flakes lesser than 100nm in size. This method can be scaled up at a cheap cost. [16]



### 2.2.2.1 Chemical Vapour Deposition

The precursor gases are pass through a preheated furnace in which either the gases diffuse together or get adsorbed onto a substrate forming a thin layer of the required substance. Factors like pressure temperature and time to complete the reaction must be regulated since they modulate the thickness and quality of film. This can method can be used at large scale to synthesize high quality films. [17]

## 2.3 Some important types of two-dimensional materials

### 2.3.1 Graphene

Graphene was the first two-dimensional element to be discovered. While graphene has been studied theoretically for more than fifty years, it was considered to be too energetically unstable to be isolated. It was first synthesized by Geim and Novoselov in 2004. Since then, owing to its outstanding mechanical, optical and electrical characteristics along with presence of massless Dirac fermion quasiparticles in graphene, it has received an outburst of research attention. [18] Eventually, it garnered the Nobel Prize for Physics in 2010 for Geim and Novoselov. Graphene has a hexagonal

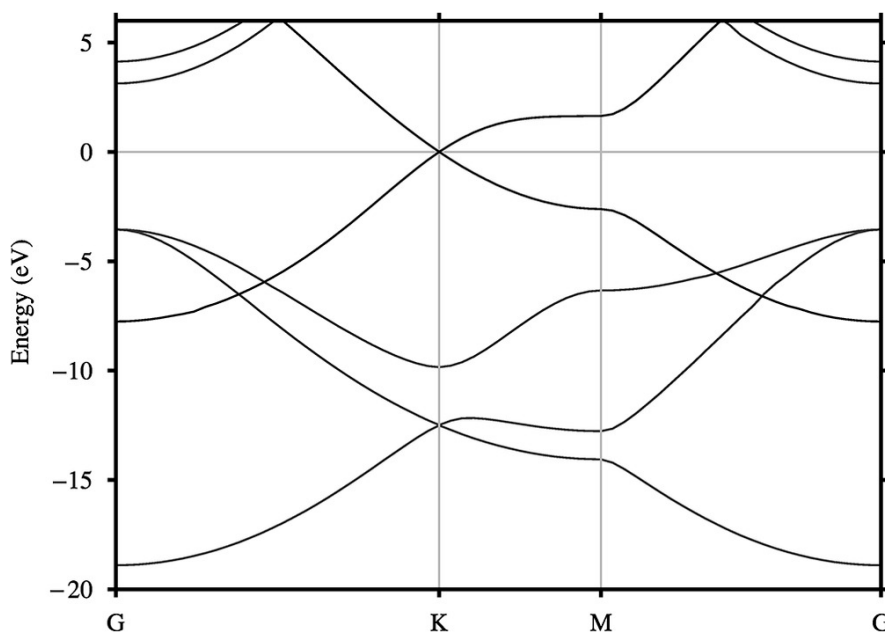


Figure 4: Band structure of graphene [19] (Creative Commons License)

structure of  $sp^2$  hybridised carbon atoms that is one atom thick and held together by covalent bonds. On observing its band structure, we can see that the conduction band and valence band overlap.

Because of its unusual band structure, electrons flow at extremely high speeds ( $\sim 1/300$  the speed of light), giving it unique features including thermal conductivity. [1]

Graphene possesses the greatest tensile strength as compared to any other material in the world. Graphene is optically transparent and 98% of visible light incident on its surface passes through it. The thickness of its ML is roughly 0.3nm. [1]

The Fermi level can be found at the Dirac point where no electronic DOS is expected to exist for charge carrier transport in the case of no electrostatic doping, according to the transfer characteristics of a graphene field effect transistor. The linear and symmetric E-k dispersion at Dirac point causes the symmetry observed around the charge neutrality point, resulting in ambipolar transport characteristics. [20]

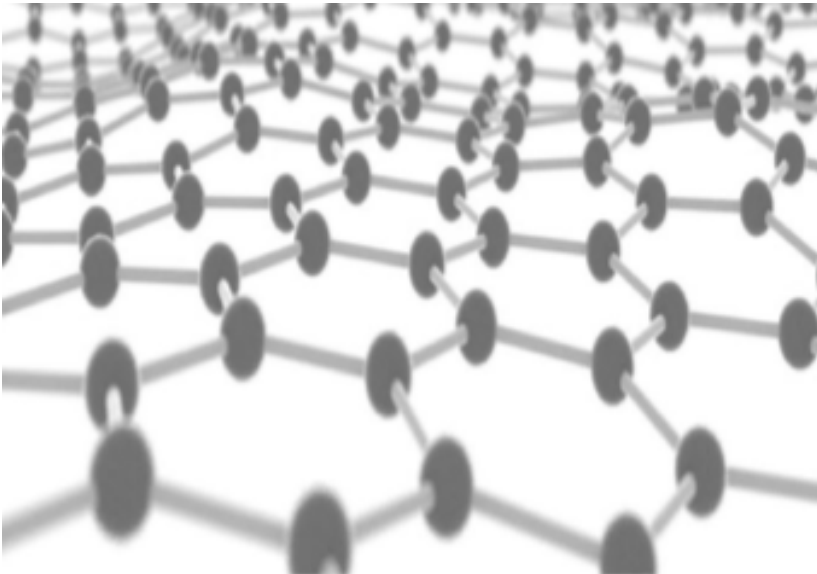


Figure 5: Graphene monolayer [21] (Creative Commons License)

### 2.3.2 Two Dimensional Transitional Metal Dichalcogenides

Transitional metal dichalcogenides have the chemical formula of  $\text{MX}_2$ . Here, M refers to a transition metal like tungsten, tantalum, bismuth, nickel and so on. X refers to chalcogen like sulphur, tellurium or selenium. [22]

In TMDCs, the bonding between atoms in the same layer is covalent and the bonding between atoms in different layers is van der Waals. Hence, TMDCs have highly anisotropic characteristics. The inplane thermal, mechanical and electrical characteristics are much greater than the out of plane characteristics. [23]

TMDC can be found in a variety of crystal structures. When restricted to a single plane, that is in 2D materials, there are 2 types of structures that affect electronic characteristics of layers – trigonal prismatic and octahedral. [24] Most phases can be turned into each other via atomic gliding of layers. [24] Some of the most commonly found TMDCs are 2H phase along with trigonal symmetry. These are semiconducting in nature and include  $\text{MoS}_2$  and  $\text{WS}_2$ . When observed in bulk, they have an indirect bandgap, that is greatest maxima of VB and the lowest minima of CB have different values of momentum. However, MLs have a direct bandgap observed in the visible spectrum. Thus, MLs can be used for optoelectronic applications. They are also used for two-dimensional transistors since their charge mobilities is in the range of 0.01 to 0.1  $\text{m}^2/(\text{Vs})$ . [22]

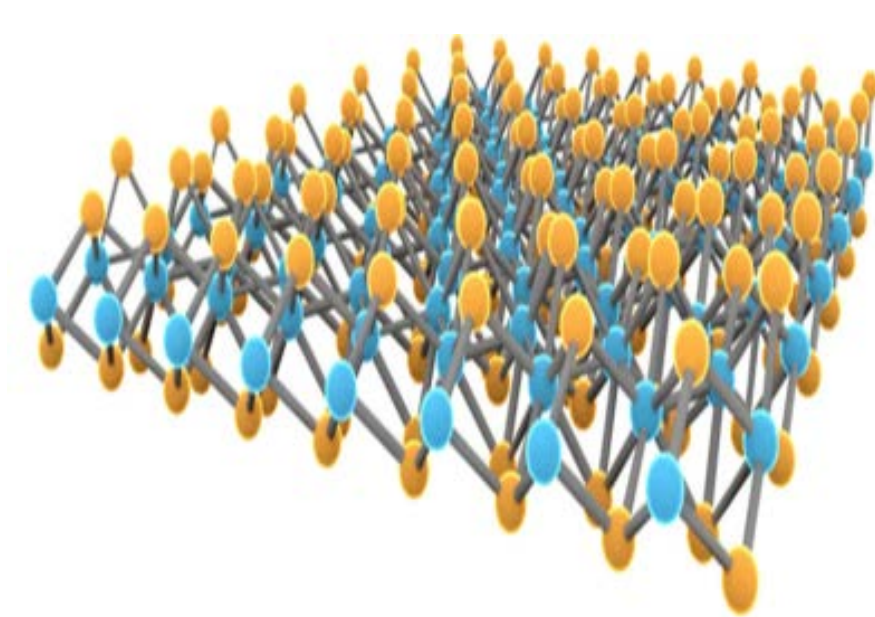


Figure 6: Two-dimensional structure of  $\text{WTe}_2$  [25] (Creative Commons License)

### 2.3.3 Xenes

Xenes are a group of 2D materials similar to graphenes, including silicenes, stanenes and germanenes. Here, the X in xenes stand for Si, Sn and Ge respectively. Xenes consist of group 13, 14 and 15 element atoms structured in a hexagonal lattice. [22] This lattice has variable amount of buckling throughout its structure, mainly due to presence of both  $\text{sp}^2$  as well as  $\text{sp}^3$  hybrid bonds. Xenes cannot be synthesized by top down approaches and have to be MLs grown on a substrate epitaxially. [1] A variety of xenes can be produced using Ag (111) as the substrate. The substrate chosen often controls the properties of the material, due to chemical reaction between the atoms and substrate. [26] Xenes

have potential uses in FETs and topological insulators, however many of the xenes are unstable in ambient conditions. [1]

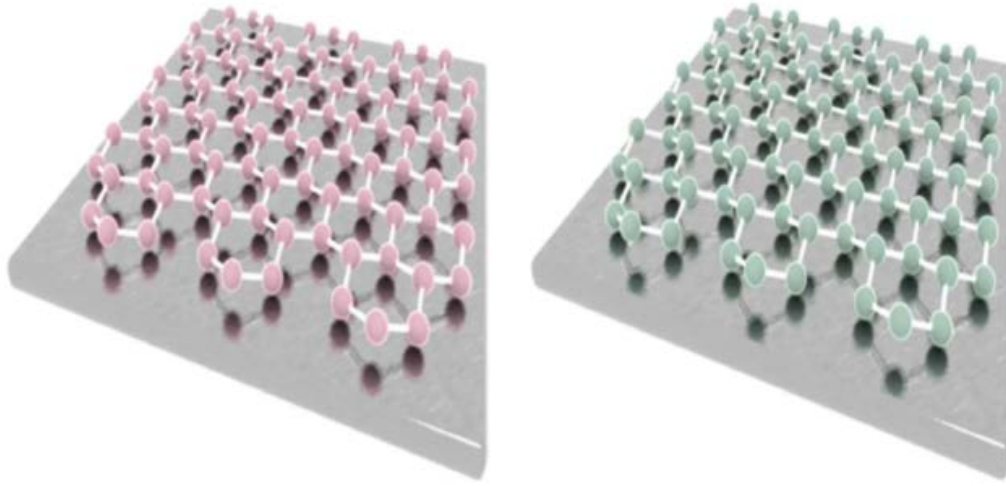


Figure 7: Buckled hexagonal structure of stanene and silicene, respectively [27] (Creative Commons License)

### 3. Molybdenum disulphide

#### 3.1 Introduction

Molybdenum sulphide is a naturally occurring transition metal dichalcogenide, which has been present in nature for millenia. In the 1950s, early research was done on producing molybdenum disulphide by reducing  $\text{MoS}_3$ , and high-temperature solution techniques. [28] Since graphene was isolated by Geim et al in 2004, research interest in two-dimensional materials was renewed. Recently, the focus has shifted to other two-dimensional materials similar to graphene, in order to handle the shortcomings of graphene and extend the potential of usage of 2D materials. Since then,  $\text{MoS}_2$  has become one of the most researched TMDC material.

#### 3.2 Properties

In monolayer  $\text{MoS}_2$ , Mo (+4) and S (2-) exist in a sandwich structure. They are held together by covalent bonding in a S-Mo-S order. [29] The sandwich layers interact with each other via weak vdW forces. The thickness of ML is roughly  $6.5\text{\AA}$ . 2D  $\text{MoS}_2$  is found to semi-conductive in nature in the trigonal prismatic molecular geometry (2H form). In the octahedral symmetry structure, 2D  $\text{MoS}_2$  is found to be metallic in nature and called the 1T form. [30]

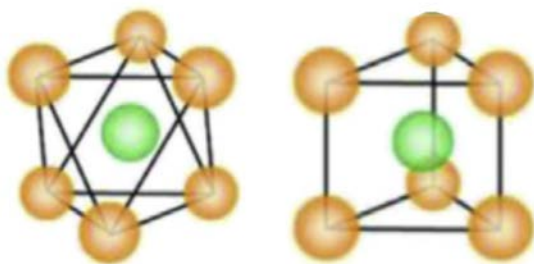


Figure 8: Types of monolayer  $\text{MoS}_2$ : 1T (left), 2H (right) [31] (Creative Commons License)

The 2H structure, which contains 2 layers/unit cell is in hexagonal symmetry, is the most common stable phase seen in nature with ABA stacking. S atoms from distinct planes are perpendicular to one other and occupy the same locations. Mo-S bond is primarily covalent, whereas S layers are held together by vdW forces and glide easily over one another. The dislocation of one of the S layers produces 1T structure with an ABC layering sequence. [32] It features a trigonal symmetry and a symmetrical Mo-Mo bond. Since 1T phases contain more exposed active sites, they improve the

electrical conductivity. The existence of filled  $d_z^2$  and empty  $d_{xy}$  and  $d_{x^2-y^2}$  orbitals in 2H gives it semiconductor characteristics. The 4  $d^2$  orbitals in 1T split into  $e_g$  orbitals rather than  $t_{2g}$  orbitals, resulting in metallic behaviour. The metallic nature of 1T is due to the two electrons occupied in  $t_{2g}$  states. [32]

2D  $\text{MoS}_2$  is great elasticity and high strength with elastic modulus of roughly 0.33 TPa. [33] When  $\text{MoS}_2$  is exposed to strain, its elasticity prevents deformation and band gap alterations in its structure. Mechanical strain, on the other hand, is employed to change the electronic properties of  $\text{MoS}_2$  and convert it from a semiconductor to a metal. [32]

Several first principles based DFT studies have been undertaken to research the electrical properties of  $\text{MoS}_2$ . The value of  $\kappa$  (high symmetry point in the first Brillouin zone) is determined by d-orbitals of Mo, and does not vary as size shrinks because it is unaffected by the number of layers. The valence band is made up of 2p orbitals of S. As a result, the bandgap between  $\kappa$  and  $\Gamma$  (another high symmetry point in the first Brillouin zone) varies, as the  $p_z$  orbital of S and d orbital of Mo, determine the bandgap. The valence band maximum point decreases below zero as the number of layers decreases, forming a new point. This new VBM will have a new and increased bandgap of 1.9eV. [32]

When doped with Cr, Cu and Sc, ML  $\text{MoS}_2$  turns to n-type semiconductor. When doped with Ni or Zn, it turns into a p-type semiconductor. When doped with Ti, it changes its doped nature according to the concentration of Ti and point of doping. It acts like p-type conductor at low concentrations below 2.04%, and at 3.57% concentration with interstitial doping, it becomes an n-type semiconductor. This is because of the strong covalent linkage between  $\text{MoS}_2$  which causes dipole moment at the surface to rise. [34]

The charge mobility of  $\text{MoS}_2$  can go upto  $0.2\text{m}^2\text{V}^{-1}\text{S}^{-1}$  at ambient temperature by using  $\text{HfO}_2$  for gate dielectric, according to Radisavljevic et al. [35] Conventionally,  $\text{MoS}_2$  FETs exhibit n-type behaviour. Monolayer  $\text{MoS}_2$  based phototransistors have great switching character, with the whole cycle of photocurrent induction and termination within 50 milliseconds, in a device developed by Yin et al. [36] The responsivity of this device can exceed that of graphene based devices, hence  $\text{MoS}_2$  can be used for devices like FETs, memory and photo-detectors.

Raman spectra is an approach to conveniently characterize for studying the evolution of structural characteristics in layered substances as they transition from 3D bulk blocks to 2D vdW bonded constructs, and they've been widely utilised to investigate graphene quality and layer number.  $\text{MoS}_2$

displays 4 active Raman modes under IR scattering. 2D monolayer MoS<sub>2</sub> exhibits two peaks representing in-plane and out-of-plane vibrations of S atoms. If the number of layers rises, then the peaks are observed to have red shift and a blue shift respectively. [30]

Since bulk form needs more energy to transfer e<sup>-</sup> from valence band to conduction band, mobility of substance is greatly improved by decreasing its thickness and introduction of a direct bandgap. MoS<sub>2</sub> can be utilized for diverse purposes via decreasing dimensions, intercalation or producing different heterostructures due to effect of the number of layers on optical characteristics.

Photoluminescence is inversely proportional to thickness of substance and can be utilised to calculate the number of layers in the material. Because of the direct bandgap at reduced thickness, the dominance of excitons reveals direct excitonic transition at point  $\kappa$ . In bulk, MoS<sub>2</sub> has a low PL intensity due to weak phonon interaction and strong excitonic absorption that is larger than the indirect bandgap. The quantum confinement of electrons in d orbitals is responsible for this remarkable behaviour. When shifting from bulk to monolayer MoS<sub>2</sub>, photoluminescence and Raman showed similar behaviour tendencies. [30]

### **3.3 Applications of MoS<sub>2</sub>**

#### **3.3.1 Medical Applications**

MoS<sub>2</sub> has been extensively studied in the field of medicine particularly for cancer: cure as well as detection. According to Liu et al, MoS<sub>2</sub>/graphene oxide nanocomposites with doxorubicin were utilized to study and cure lung cancer in mice. [37]

By engineering defects in quantum dots of MoS<sub>2</sub>, Ding et al were able to kill cancer cells the sulfur defects caused a rise in oxidative stress, that is, disturbed the balance between formation of reactive oxygen free radicals and antioxidant defenses of the body. [38] This helped inhibit the growth of cancer cells.

In regards to cancer detection, Zheng et al were able to develop a MoS<sub>2</sub> field effect transistor sensor to sense traces of H<sub>2</sub>O<sub>2</sub> in cells. Photoluminescence were able to detect breast cancer by recording a red shift of 16 nanometers for the biomarker of breast cancer. [39]

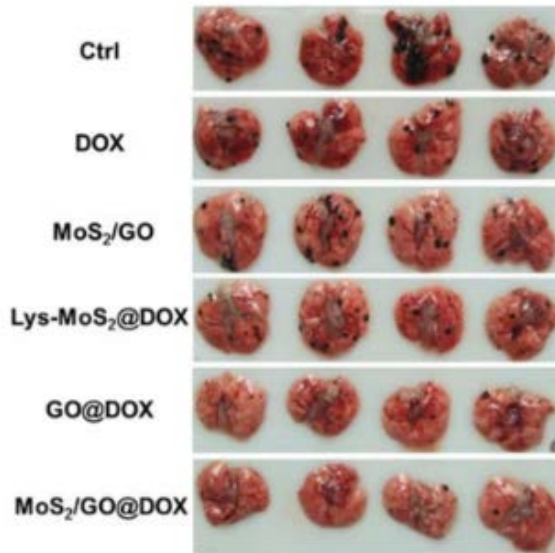


Figure 9: Effect of various agents on cancer cells in mice [37] (Creative Commons License)

### 3.3.2 Electronic Applications

Two dimensional MoS<sub>2</sub> FETs can be utilized as operational amplifiers. Using amorphous Si and MoS<sub>2</sub>, Esmaili-Rad and team were able to create a highly efficient and quick photodetector. Choi et al developed a MoS<sub>2</sub>-organic heterostructure image sensor with a simple architecture that is akin to a human vision system. This neuromorphic image sensor produces a cleaner output, with reduced noise and no redundant input information. [40]

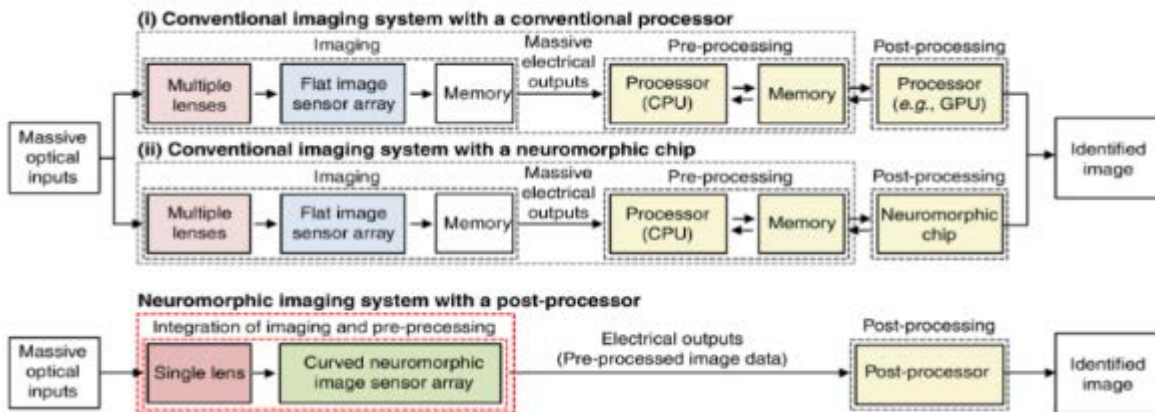


Figure 10: 1. Block diagram of conventional imaging system, 2. Neuromorphic imaging device [40] (Creative Commons License)

The trapping effect in MoS<sub>2</sub> stack causes delayed decay of the photocurrent and nearly linear generation of photocurrent, which depends on the time taken, which makes this image sensor possible. [40]



Sulphur treatment in alcohol improved back gate MoS<sub>2</sub> transistors according to researched conducted by Sahoo and team, with gate lengths ranging from 5000 to 800 Å and contact resistances of 1.3K Ω. [41]

### 3.3.3 Energy Applications

MoS<sub>2</sub> has been used in a variety of solar cells and Li-ion cells. By utilizing it as a buffer, Dey et al were able to develop a solar cell with improved stability and efficiency. [42] Another team was able to use the MoS<sub>2</sub>/silicon heterojunction to enhance conversion rate in solar cells by more than four times. [43] Huang et al used an anode made of MoS<sub>2</sub> in Li-ion cells. After 50 cycles, this battery was able to maintain a reversible capacity of 786x10<sup>-3</sup>Ahg<sup>-1</sup> at 10<sup>-1</sup>Ag<sup>-1</sup> with a capacity of 1.103 AH. [44]

## 4. Point Defects

### 4.1 Introduction to defects in 2D materials

The structures of 2D materials, like other materials, invariably contain a variety of defects, such as vacancies, adatoms, grain boundaries, and substitutional impurities, all of which have a significant impact on their properties. Due to scattering from localised defects and GBs, the carrier mobility of graphene in electronics is greatly influenced by the amount of defects inside as well as its crystalline grain size. It has been shown that even a tiny quantity of imperfections in mechanically exfoliated graphene can significantly reduce carrier mobility. [45] Due to the development of a greater number of defects and grain boundaries, graphene produced by CVD often has poorer mobility than those that are mechanically exfoliated. Similarly, structural flaws hinder carrier mobility in TMDs devices, limiting their electrical and optoelectronic performance.

### 4.2 Types of defects in 2D materials

In two-dimensional materials, defects that occur can be intrinsic or extrinsic. The basis of classifying defects is mainly the dimensionality of defects. There are two types of defects:

- a. Zero dimensional defects: Vacancy, Adatoms, SW defects, substitutional impurities
- b. One dimensional defects: Line defects, edges, grain boundaries [45]

#### 4.2.1 Zero Dimensional

##### 4.2.1.1 Vacancies

Vacancies along with the anti-sites that develop on them are the most basic and common flaws in 2D materials. Apart from the simple vacancy (where an atom is missing from the lattice structure), when more than two adjacent atoms are absent, bigger and more complicated defect structures occur. In graphene, double vacancies can be produced via coalescence of two single vacancies or by removing two adjacent atoms. TMDs can also have several types of vacancy flaws. MoS<sub>2</sub> has various types of defects: S vacancy (one S atom missing referred to as  $V_S$ ), S<sub>2</sub> vacancy (two S atoms missing, referred to as  $V_{S_2}$ ), or Mo vacancy (one Mo atom missing referred to as  $V_{Mo}$ ). [45]

Some vacancy flaws, on the other hand, are unstable, causing defect rebuilding. Single vacancy experiences jahn-teller effect in graphene, resulting in the creation of a 9-membered and 5-membered ring. [46]

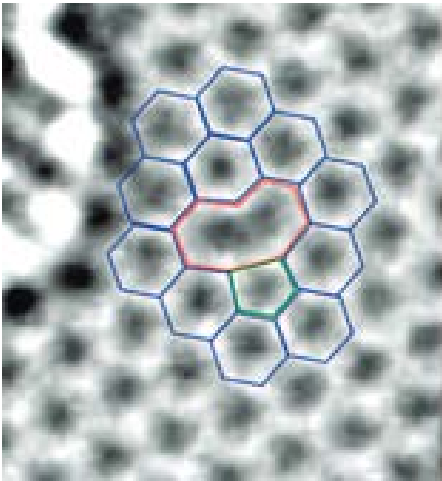


Figure 11: Reconstructed vacancy in graphene with atomic configuration - 9 and 5 membered ring [46] (Creative Commons License)

#### 4.2.1.2 Adatoms

Adatom are formed when foreign atoms are adsorbed onto 2D materials. Only physical adsorption happens when the contact between the foreign atom and 2D materials is weak. Covalent bonding between the foreign atom and the closest atom of 2D materials leads to chemical adsorption if the interaction force is greater. Chemisorption occurs primarily in three positions in graphene: in C-C bond, above C atoms, and entrapped by structural defects. [45]

#### 4.2.1.3 Stone Waller defect

Stone Waller defects are simple defects, which are created by reconstructing graphene lattice (switching between pentagons, hexagons, and septagons) with  $90^\circ$  rotations of carbon-carbon bonds in  $sp^2$ -hybridized hexagonal C units. It can be created by cooling down quickly from a high temperature or by exposing it with electron beams. [45]

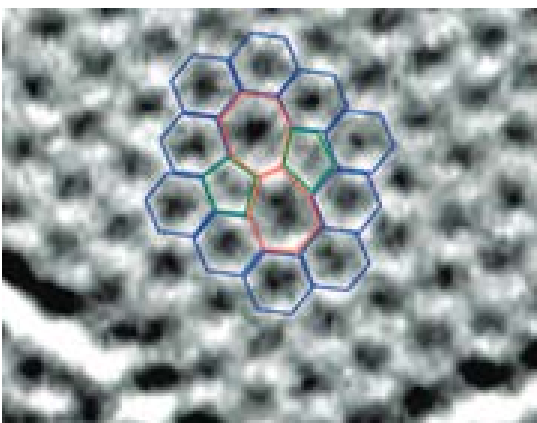


Figure 12: SW defect in graphene [46] (Creative Commons License)

#### 4.2.1.4 Substitutional defect

Substitutional impurities is the one of forms in which foreign atoms can be introduced into the crystal structure of two-dimensional materials. Because of their strong covalent bonding, substitutional dopants are predicted to be extremely stable. The Fermi level and the electrical structure of graphene can be changed by replacing C atoms with transition metal impurities, B or N atoms. [45]

### 4.2.2 One Dimensional

#### 4.2.2.1 Line Defects

Dislocations (or line defects) are caused by stresses experienced by the material during deformation. When material is deformed beyond the elastic limits, dislocation lines emerge, and extra-atom lines demarcate regions in the lattice where movement of one portion of crystal relative to another has occurred. The additional plane of atoms is the dislocation line, and the structure is deformed in its immediate vicinity. A pair of pentagon–septagons rings (5|7) is the most frequent dislocation in graphene. [22]

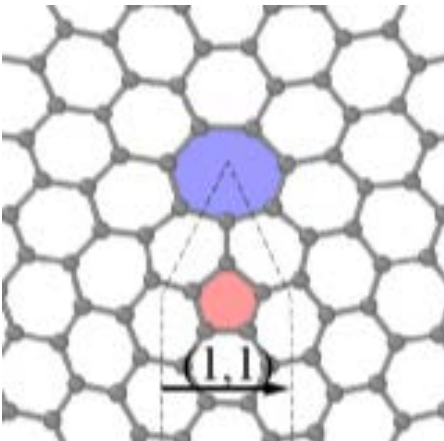


Figure 13: (1,1) Line defect in graphene [22] (Creative Commons License)

#### 4.2.2.2 Grain Boundary

Large-scale 2D material films produced via chemical vapour deposition are generally polycrystalline, and grain boundaries are a common form of defect that can have a significant impact on the characteristics of these materials. Grain boundary is a typical planar defect in 3D materials that separates two grains with different orientations. Misorientation is generally represented by an angle

and is a key characteristic of grain boundary. The grain boundary is a line array of dislocation cores in the 2D lattice. [45]

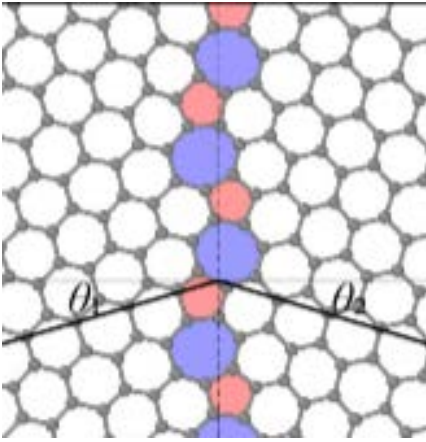


Figure 14: Grain boundary defect [22] (Creative Commons License)

#### 4.2.2.3 Edges

Two dimensional materials have various types of edge terminations. These affect the structure as well as the characteristics of the materials. The manually exfoliated graphene sheets exhibit crystal cleavage characteristics since it is a perfect single crystalline structure. Most graphene angles are dispersed at roughly  $n \times 30^\circ$ , where  $n$  denotes a whole number in the range of 0 to 6, implying that graphene has zigzag or armchair edges, according to studies by You et al. [47]

### 4.3 Defects observed in MoS<sub>2</sub>

#### 4.3.1 Point Defects

There are 4 different forms of vacancies and 2 different types of antisite faults commonly observed in the point defects of MoS<sub>2</sub> structure. The mono vacancy of S ( $V_S$ ), divacancy of S pairs ( $V_{S_2}$ ), and vacancy complex consisting of 1 molybdenum vacancy with three S vacancies ( $V_{MoS_3}$ ) and molybdenum vacancy with three adjacent disulphur pairs ( $V_{MoS_6}$ ) are among the vacancy defects. The antisite defects found are MoS<sub>2</sub> (molybdenum atom replacing S<sub>2</sub>) and S<sub>2</sub>Mo (S<sub>2</sub> column substituting

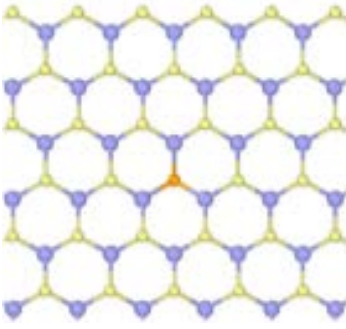


Figure 15: Sulphur monovacancy  $V_s$  point defect [48] (Creative Commons License)

molybdenum atom).  $V_s$ , the defect with smallest enthalpy of formation (from DFT calculations), is the most commonly observed defect and both the antisites, with higher enthalpy of formation than other defects, are rarely observed. [22]

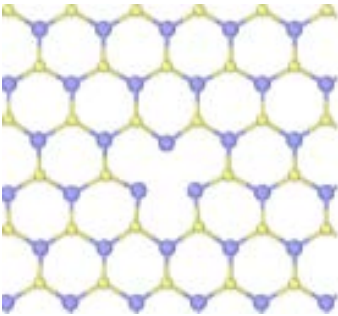


Figure 16: Vacancy complex  $V_{MoS3}$  [48]

According to atomistic imaging and spectroscopy studies conducted by Hus et al, substituting metal atom into sulphur vacancy creates non-volatile shift in resistance, which can be used in high-density information memory, computing and reconfigurable devices. [49]

#### 4.3.1 Dislocations and GBs

MoS<sub>2</sub> dislocation cores are usually shaped like a four-sided top and feature concave 3D polyhedra of consisting of multiple elements. A common dislocation structure in 2D materials comprised of hexagonal rings is the 5|7 dislocation core. These pairs have both Mo-rich and S-rich types with homoelemental links due to the presence of multiple elements. Burger vector of a 4|8 dislocation in MoS<sub>2</sub> is greater in magnitude than that of a 5|7 dislocation, resulting in higher elastic deformation energy. The former is unstable and generally breaks down into 2 dislocations of the latter type, where there is a Mo-rich and S-rich core to maintain balance. [48]

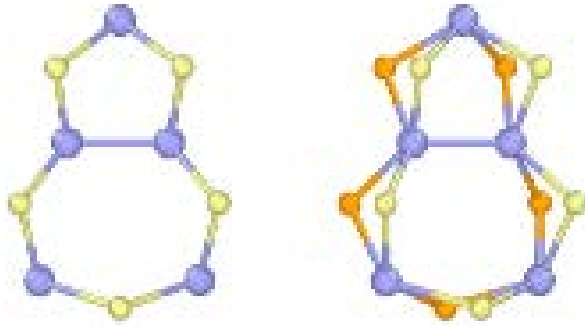


Figure 17: 5|7 dislocation in  $\text{MoS}_2$  [48] (Creative Commons License)

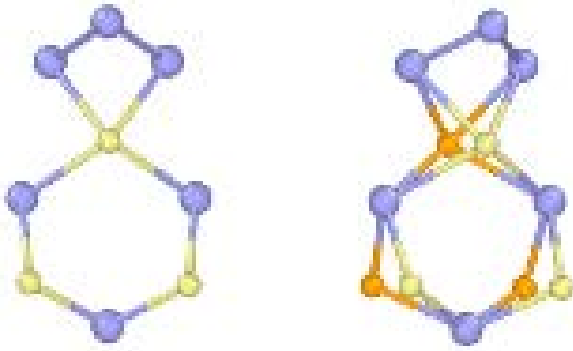


Figure 18: 4|6 dislocation in  $\text{MoS}_2$  [48] (Creative Commons License)

$\text{MoS}_2$  has two different types of grain boundaries: asymmetric (asym-GB) and symmetric (sym-GB). Symmetric grain boundaries which are misoriented by  $60^\circ$  exhibit 4-fold rings which all share a point at a sulphur divacancy. This is called the 4|4P grain boundary. In 4|4E GB, the rings can share an edge. Symmetric grain boundaries are polar since there is a deficiency of one of the elements. Asymmetric grain boundaries are non-polar since both elements are equal in quantity. Energy of grain boundary over its length has a positive linear relationship with the tilt angle until a large value of tilt value is reached. [48]

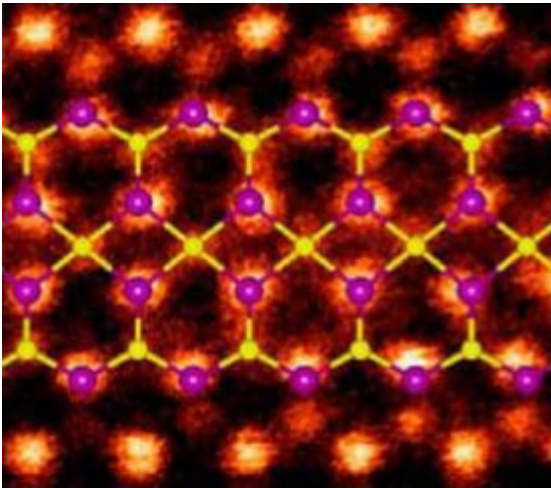


Figure 19: 4|4P 60° grain boundary structure [48] (Creative Commons License)

#### 4.4 Why study point defects?

Modern microelectronics revolves around the field of band engineering. The path of customising and tweaking the lattice structure originates from doping, defects and heterostructuring to alter the atomic structure. A vast chunk of current electronics is built on Si FETs, optoelectronic devices made of Gallium arsenide, and LEDs of Gallium nitride and may be attributed to the remarkable triumph of modern band engineering. Although 2D material systems may hold the promise of future electronics, its band modulation/engineering techniques have not been investigated as comprehensively as the techniques responsible for mature silicon semiconductor systems. Despite the fact that 2D materials are shown to have unique and lucrative characteristics in transportation and solar applications, there is still a significant distance between laboratory research that is being performed and industrial use profiting off that research. Since structure disorder is a major aspect in most semiconductors, the same difficulty must be researched in the synthesis of 2D materials as well as scaling the same to industrial uses. [50]



## 5. Density Functional Theorem

### 5.1 Need for Computational Studies

Due to the fast advancement of contemporary computational chemistry, there is a rising need to comprehend the microscopic mechanisms that determine the characteristics of molecular and solid materials at the atomic level. The rules of quantum mechanics regulate interactions between atoms and electrons, necessitating the development of precise and efficient computer techniques to solve quantum-mechanical equations. [51]

Computational chemistry approaches have grown in significance in recent years, as established by their fast expanding applications in a wide range of fields, including molecular structure and property calculations, pharmaceutical drug design, and invention of new materials, among others. The size of the systems that one is able to analyse computationally has risen because of this. Hence, this has created even more need for large-scale applications. This is occurring because bigger molecular systems exhibit fascinating phenomena and have significant consequences in current biochemistry, biotechnology, and nanotechnology. [51]

### 5.2 Origin of Computational Studies

The density functional theory (DFT) proposed by Kohn and Sham in 1965 was a game-changer in these endeavours, and it has had an incomparable influence on a wide range of intriguing and difficult issues in computational chemistry during the last couple of decades. When benchmarked against other wave-function-based techniques like CC theory or MP perturbation theory, DFT's true strength is its favourable price/performance ratio. As a result, DFT can be utilized to study large-scale molecular and solid systems with adequate precision, extending the predictive potential of electronic structure theory. As a result, DFT is currently by far the most commonly utilised approach for determining electrical structure. [51]

Recent advances in ML techniques have allowed for molecular dynamics simulations at a large scale with ab initio precision, and this technology has been used to a wide range of applications. The considerable parallelism afforded by powerful computer networks and scalable programming approaches on high performance computing have spurred enormous advancements in the capabilities of computational chemistry simulations over the last few decades. The diversity of relevant data structures and methods, as well as the often occurring intrinsic sequential control, make optimal

utilisation of a large number of processors challenging. Hence, designing parallel architecture with good efficiency is a demanding task.

By using the monoparticle Green's function, the Green's function technique gives information similar from that obtained by solving the Kohn-Sham equation. Lowered scaling in the computations of metallic systems is a significant benefit of the MST technique. The multiple scattering theory technique demonstrates the capability of massively parallel supercomputers to model increasingly complex materials and provides a dependable and accessible method for large-scale ab initio simulations of metals and alloys. [52]

The ab initio molecular dynamics method has been widely used to investigate the real-time information of electronic systems. Due to the presence of static correlation, it is still exceedingly difficult to forecast the electrical characteristics of radical systems using ab initio DFT calculations. DFT framework has undergone another wave of rapid evolution in combination with HPC and ML approaches. DFT methods with more efficient algorithms and greater accuracy are likely to be released in the near future. [51]

### 5.3 Many Body Problem

At the atomic level, Quantum Mechanics govern the behaviour of particles. If we wish to study a phenomenon in a substance, such as electromagnetism, we must first study the interaction behaviour of the material's essential elements, that is, nuclei and electrons. All of the material's properties are determined by the interaction between these electrons and ions. The solution to the time-independent Schrödinger equation explains the behaviour of the fundamental elements. [53]

$$H\psi = E\psi \quad (5.1)$$

Where,  $H$  is the Hamiltonian function,  $\psi$  refers to wave function and  $E$  refers to the energy eigenvalue of the system known as total energy of the system. For eg, to solve equation 5.1 for a H atom, we can exactly solve it because it is a simple system with a single electron and a single proton.

However, when we progress to even more complicated systems, solving this equation becomes more difficult due to the high amount of ions and electrons. We must address the complex interactions

between electrons and ions in typical materials due to the large quantity of electrons and ions. Hence, Hamiltonian can be given by

$$H = T_E + T_I + V_{II} + V_{EE} + V_{IE} \quad (5.2)$$

$$H = -\frac{\hbar^2}{2m_e} \sum_i \frac{\partial^2}{\partial \mathbf{r}_i^2} - \frac{\hbar^2}{2M} \sum_l \frac{\partial^2}{\partial \mathbf{R}_l^2} + \frac{1}{2} \sum_{\substack{l,l' \\ l \neq l'}} \frac{e^2 Z_l Z_{l'}}{4\pi \epsilon_0 |\mathbf{R}_l - \mathbf{R}_{l'}|} + \frac{1}{2} \sum_{\substack{i,j \\ i \neq j}} \frac{e^2}{4\pi \epsilon_0 |\mathbf{r}_i - \mathbf{r}_j|} - \sum_{\substack{l,l' \\ l \neq l'}} \frac{e^2 Z_l}{4\pi \epsilon_0 |\mathbf{r}_i - \mathbf{R}_l|} \quad (5.3)$$

Where in equation 5.2,  $V_{II}$  refer to potential energy of two nuclei,  $V_{IE}$  to that of nuclei-electron system and  $V_{EE}$  to that of two electrons;  $T_E$  refers to kinetic energy of electrons,  $T_I$  to that of ions. In equation 5.3,  $i$  refers to nuclei and  $l$  refers to electrons;  $m_e$  is the mass of electron and  $M$  is the mass of nuclei;  $Z_l$  and  $Z_{l'}$  refer to the charges present on the various nuclei; and  $\mathbf{r}_i - \mathbf{r}_j$  refers to distance between two electrons,  $\mathbf{R}_l - \mathbf{R}_{l'}$  refers to that between two nuclei and  $\mathbf{r}_i - \mathbf{R}_l$  refers to that between nuclei and electron. Since solving this equation is based on the fundamentals, we are said to be following first-principles. By solving equation 5.2 with the value of Hamiltonian obtained from 5.3, we obtain the total energy of the system, and then we obtain ground state behaviour of the particular substance at equilibrium, from the calculated total energy.

But practically, as we progress from smaller, easier systems like H atom to bigger, more complicated systems, solving equation 5.1 gets harder because the amount of complex interactions to account for grows, as the number of electrons and ions grows. As a result, to solve the complexity, we use several approximations that attempt to simplify the problem.

## 5.4 Wave Function Based Method To Solve Many-Body Equation

### 5.4.1 Hohenberg-Kohn Theory

Hohenberg and Kohn demonstrated that all of the ground state features of systems with a large number of electrons can be computed using an electron density functional. Because the density of electrons is dependent on only three factors, the computations are simplified.

**Theorem 1:** External potential of a system of interacting particles  $V_{\text{ext}}(\mathbf{r})$  is determined uniquely, except for a constant, by ground state particle density  $n_0(\mathbf{r})$ .

**Theorem 2:** For any particular  $V_{\text{ext}}(\mathbf{r})$ , ground-state energy functional of system gives the lowest energy if and only if input density is the true ground-state density.

The Kohn-Sham ansatz is defined as the replacement of a challenging interacting many-body system obeying the Hamiltonian with a simpler auxiliary system and depends on 2 assumptions:

1. The ground state density of an auxiliary system of non-interacting particles can be used to describe the exact ground state density.
2. The auxiliary Hamiltonian is selected to have the typical kinetic operator as well as an effective local potential  $V_{\text{eff}}^\sigma(r)$  acting on a  $\sigma$  spin electron at  $r$  point.

$$\widehat{H}_{\text{aux}}^\sigma = -\frac{1}{2}\nabla^2 + V_{\text{eff}}^\sigma(r) \quad (5.4)$$

The ground state of Kohn-Sham functional can be given as:

$$E_{\text{KS}} = T_s[n] + \int dr V_{\text{ext}}(r)n(r) + E_{\text{Hartree}}[n] + E_{\text{II}} + E_{\text{xc}}[n] \quad (5.5)$$

Here,  $n(r)$  refers to electron density.  $T_s[n]$  refers to independent particle kinetic energy.  $V_{\text{ext}}(r)$  refers to external potential due to nuclei.  $E_{\text{xc}}$ , which refers to exchange correlation energy, contains the many body effects from exchange effects as well as correlation effects.  $E_{\text{II}}$  refers to interaction energy between 2 nuclei.  $E_{\text{Hartree}}$  refers to Coulomb interaction energy of  $n(r)$ . [54]

We can calculate electron density as:

$$n(r) = \sum_{\sigma} n(r, \sigma) = \sum_{\sigma} \sum_{i=1}^{N_{\sigma}} |\psi_i^{\sigma}(r)|^2 \quad (5.6)$$

For a system of  $N$  independent electrons with a single electron in ground state for each orbital  $\psi_i(r)$  with minimum eigenvalue of Hamiltonian as  $\varepsilon_i$ . We can calculate kinetic energy as:

$$T_s = \frac{1}{2} \sum_{\sigma} \sum_{i=1}^{N_{\sigma}} |\nabla \psi_i^{\sigma}(r)|^2 \quad (5.7)$$

We can also calculate Hartree energy as:

$$E_{\text{Hartree}}[n] = \frac{1}{2} \int d^3r d^3r' \frac{n(r)n(r')}{|r-r'|} \quad (5.8)$$

By minimizing the ground state Kohn-Sham energy functional wrt density, we can solve the auxiliary system for the ground state. Hence, we get the Kohn-Sham equations:

$$(H_{\text{KS}}^\sigma - \varepsilon_i^\sigma) \psi_i^\sigma(r) = 0 \quad (5.9)$$

$$\widehat{H}_{\text{KS}}^\sigma(r) = -\frac{1}{2}\nabla^2 + V_{\text{KS}}^\sigma(r) \quad (5.10)$$

$$V_{\text{KS}}^\sigma(r) = V_{\text{ext}}(r) + \frac{\delta E_{\text{Hartree}}}{\delta n(r, \sigma)} + \frac{\delta E_{\text{xc}}}{\delta n(r, \sigma)} = V_{\text{ext}}(r) + V_{\text{Hartree}}(r) + V_{\text{xc}}^\sigma(r) \quad (5.11)$$

These are in the form of an independent particle equations with a potential which is self-consistent with the resulting density. These are independent of approximating  $\text{Exc}[n]$ , which if known, gives rise to the precise ground state density and energy for the interacting system. Eigenstates which define the charge density, determine  $V_{xc}$  and  $V_{Hartree}$ . Hence, the solution to the Kohn-Sham equations has to be found self-consistently.

Given below, is a flowchart of self-consistent Kohn-Sham calculation:

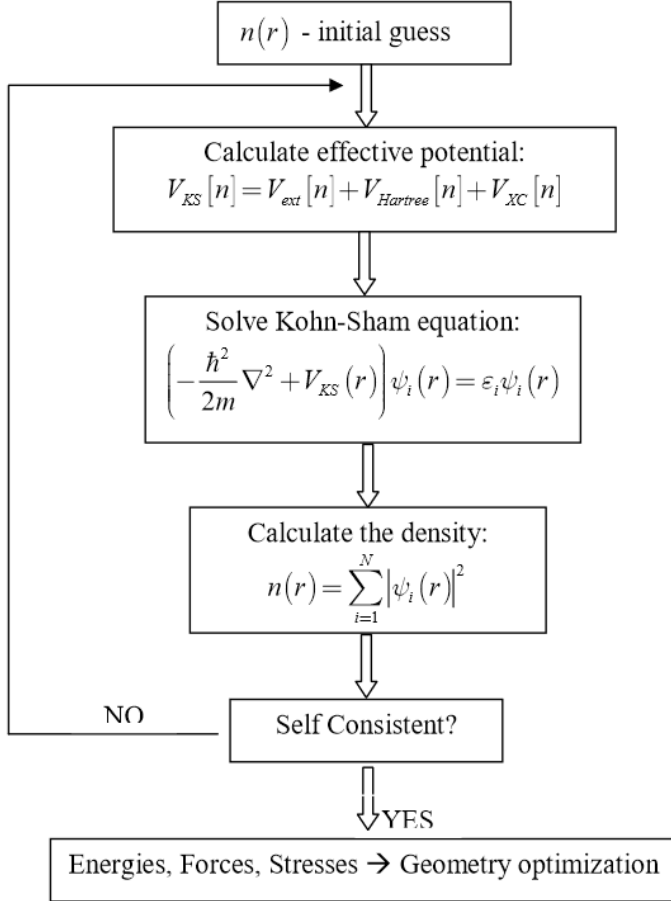


Figure 20: Flowchart of self-consistent Kohn-Sham calculation [54]

To begin, an initial estimate, like that of superposing charges of atoms, is taken. Then, using a sum of the occupied Kohn Sham orbital, we procure a charge density functional. Then, we calculate the Hartree and exchange-correlation potentials. The whole process has to be replicated till we obtain convergence of values. But practically, new charge density is mixed with the previous one so that we can prevent instable values.

After obtaining charge density convergence, we compute forces using Hellmann-Feynman theorem and shift ions towards equilibrium position and each time they are shifted, we execute self-consistent-calculation to find a new charge density functional according to the new atomic configuration. Ions shifted till the forces are minimal and the system is at geometrical equilibrium. Then, all important

properties can be obtained from equilibrium energy and density. Next, we use techniques like local density approximation (LDA) and generalized gradient approximation (GGA) to calculate the exchange-correlation potential, from which we can derive the exchange-correlation functional. [54]

GGA negates the pitfalls of LDA by considering density as well as the gradient of density to study the exchange correlation energy. Since, it considers gradient of density, GGA works better for density inhomogeneity. Simplifying calculation requires exchange correlation energy and force to be parameterized analytical function. [55]

Using pseudopotentials, we can streamline computations by defining only valence electrons under the assumption that core electrons are fixed and their wave function don't need to be considered. Since GGA doesn't consider van der Waals forces from long-range electron interactions. Hence, a term  $E_{disp}$  is added to the total energy. [56]

## 6. Results

### 6.1 Background

We study the effects of inducing point defects in the structure of 2D materials using Quantum Espresso. In the PWscf package of Quantum Espresso, we utilize a plane-wave basis set along with pseudopotentials to perform self-consistent calculations of electron structure characteristics within density functional theory. Using bands package, we plot the band structure of the material sample.

### 6.2 Computation Process

We use norm-conserving pseudopotentials, developed by researchers at Fritz Haber Institute of the Max Planck Society, for performing first principles based DFT calculations. We have picked molybdenum disulphide ( $2H-MoS_2$ ) as the material of choice to study point defects as it is one of the most representative of materials among several TMDCs.

The flowchart of simulation process is given below.

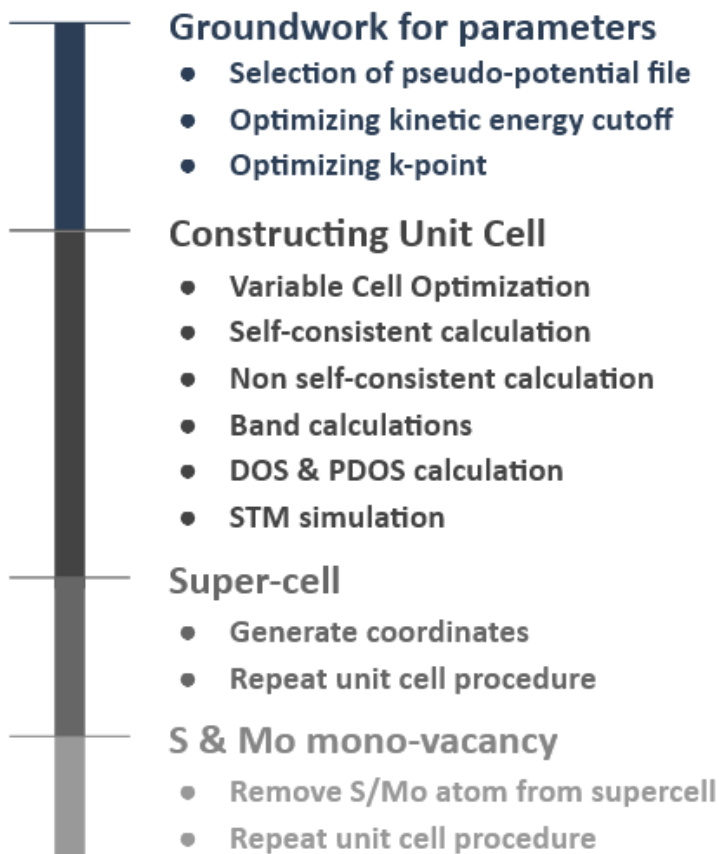


Figure 21: Flowchart of unit cell optimization

Using Quantum Espresso, we simulate a unit cell of MoS<sub>2</sub> and perform self-consistent calculations in order to optimize the structure of the unit cell.

The self-consistent field method is an iterative technique of obtaining the electronic characteristics of material. SCF calculates the difference in total energy while altering electron density differentially to estimate ground-state electron density. The computation is complete when the energy hits the global minimum and achieves convergence in its value.

The value of convergence threshold on total energy is kept at  $10^{-8}$  Ry for our purposes. When the difference between two consecutive values of final energy is below this convergence threshold, then the calculation is stopped. The Bravais lattice is custom defined and kept free. The number of electronic bands is kept at 100. The maximum number of iterations in a SCF step is kept at 300. A Davidson iterative diagonalization with overlap matrix is used with mixing factor of 0.7.

We enable Grimme's dispersion correction to take into account the presence of long-range van der Waals effect in the system. Initial parameters of cell parameters and atomic positions are taken from the Material Projects website.

After selecting the FHI norm conserving pseudo potential files for molybdenum and sulphur, we perform kinetic energy cutoff optimization. The greater the value of kinetic energy cutoff, the greater is the definition of the wave function. Assuming 10 k-points for the first round of self-consistent calculations, we calculate energy for different values of kinetic energy cutoff from 10 to 150 Ry at intervals of 10 by performing self-consistent field calculations.

In Figure 21, we can see that the graph converges to a value at kinetic energy cutoff for wavefunction value of 60 Ry. Hence, we use this value in the next iteration of self-consistent field calculations. The kinetic energy cutoff for charge density is set to 10 times the kinetic energy cutoff for wavefunctions. Hence, it is set to 600 Ry.



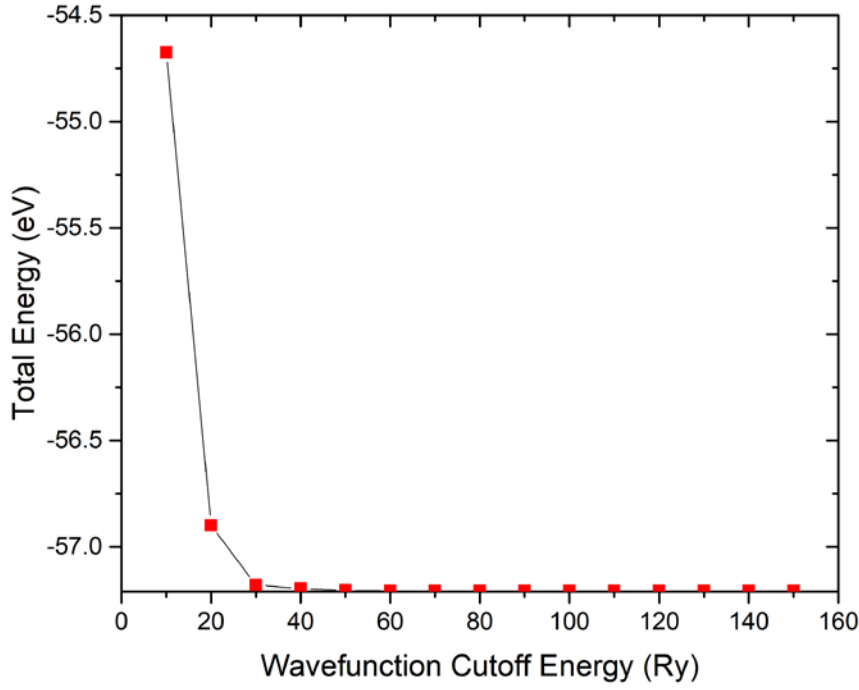


Figure 22: Optimization of Kinetic Energy Cutoff

Next, we optimize the value of k-points. Bloch's theorem states that integrals in real space over the system spread infinitely over space are substituted by integrals in reciprocal space over the finite first Brillouin zone. Further, such integrals are computed by adding values of the integrand at a limited no. of points in the first Brillouin zone. These points are together called the k point mesh and a sufficient density of this mesh is required to ensure that the calculation converges.

We try to optimize k point by sampling different values of Monkhorst-Pack grid, which defines k-points as distributed evenly in the first BZ, parallel to the reciprocal lattice vectors. Since we are performing calculations for a 2D material, the number of k points in Z direction is kept as 1. The Monkhorst-Pack grid of  $N \times N \times 1$  is iterated to calculate values of total energy at different values of N from 2 to 20.

In Figure 22, we can see that the graph converges to a value of N at 10. Hence, the Monkhorst Pack grid we'll use is a  $10 \times 10 \times 1$  pack.

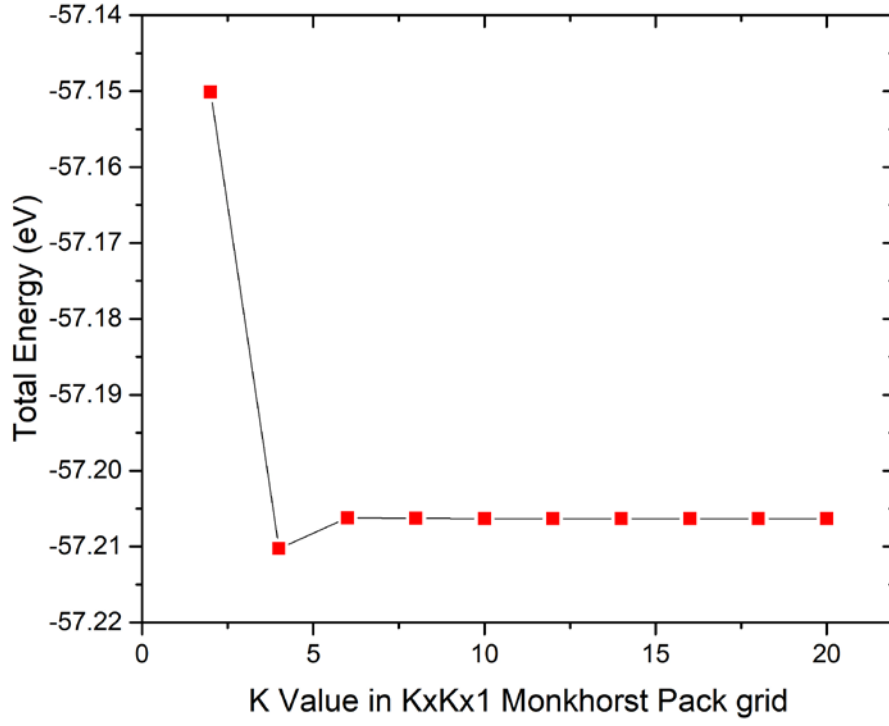


Figure 23: Optimization of Monkhorst-Pack Grid

Now that we've optimized k points and kinetic energy cutoff, we'll proceed to optimize the lattice parameter of the unit cell.

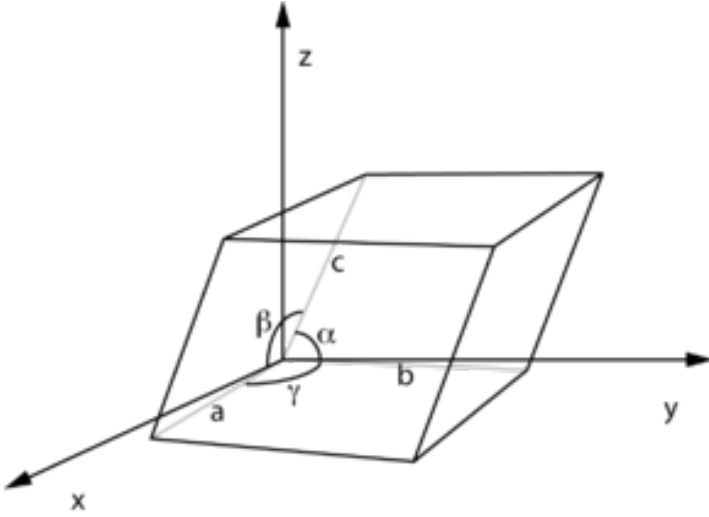


Figure 24: Unit cell definition using parallelepiped with lengths  $a$ ,  $b$ ,  $c$  and angles between the sides given by  $\alpha$ ,  $\beta$ ,  $\gamma$

In the above figure, an example of a unit cell in the form of a parallelepiped is shown. In our calculations, we aim to optimize the cell parameter 'a' and optimize the rest of cell parameter with the vrelax module of PWscf package of Quantum Espresso.

We calculate total DFT energy for different values of lattice parameter from 5.5 to 6.05 Bohr at intervals of 0.05 Bohr by performing self-consistent field calculations and plot total energy against the lattice parameter.

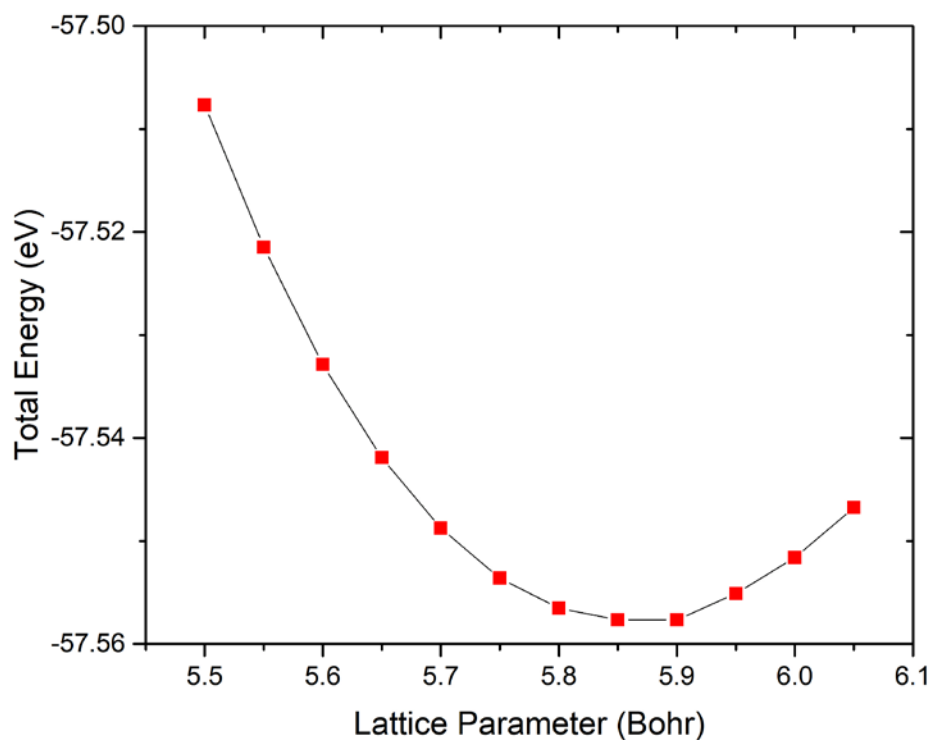


Figure 25: Optimization of Lattice Parameter

In Excel, we obtain the equation of the curve fitting all the data points. Once we obtain this curve, we use Wolfram Alpha, an online computational knowledge engine, to compute the global minimum of the equation. The point of minimum is obtained at 5.8578 Bohr.

Now that lattice parameter  $a$  is optimized, we optimize other cell parameters and atomic positions via the `vc-relax` module of the `PWscf` package of Quantum Espresso.

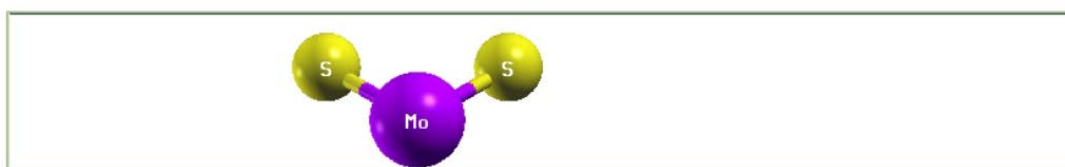


Figure 26: Side view of 1x1x1 MoS<sub>2</sub> unit cell, visualized in Xcrysden

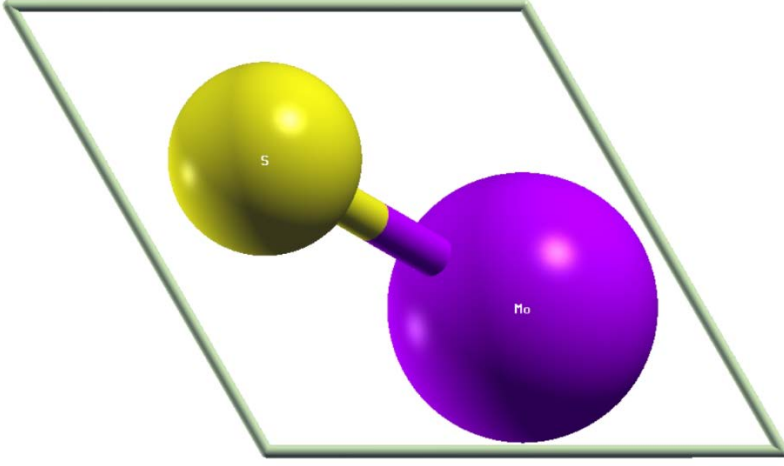


Figure 27: Top view of 1x1x1 MoS<sub>2</sub> unit cell, visualized in Xcrysden

The vcrelax package of PWscf relaxes the unit cell and allows changing of the cell parameters to ensure that unit cell is under near zero stress. To relax all the parameters of the unit cell, the Broyden-Fletcher-Goldfarb-Shanno quasi-Newton algorithm was applied to the cell dynamics of the unit cell. We also restrict the relaxation of cell parameters to the X and Y plane. After performing the cell relaxation, we obtain the final cell parameters and atomic positions of the 3 atoms. In the final iteration, pressure becomes zero. We obtain value of highest occupied energy level as -1.1973eV and value of lowest unoccupied level as 0.7318eV. Since bandgap is the difference between these two values, we obtain a bandgap of 1.98eV, which is close to the theoretical value of 1.8eV for 2D MoS<sub>2</sub> from literature. [53]

The Fermi level is equal to the average of the value of the highest occupied energy level and value of lowest unoccupied level and we get a Fermi level of -0.11eV.

Next, we proceed to calculate the band structure of the unit cell. Before that, we proceed to perform non-self consistent field calculations. Then we use the bands calculation feature of PWscf package which computes the Kohn-Sham states for the a given set of k-points. The k-points given here are the high symmetry path,  $\Gamma$ -K-M- $\Gamma$ , with k-points obtained from the 'K-Path selection' feature in Xcrysden.

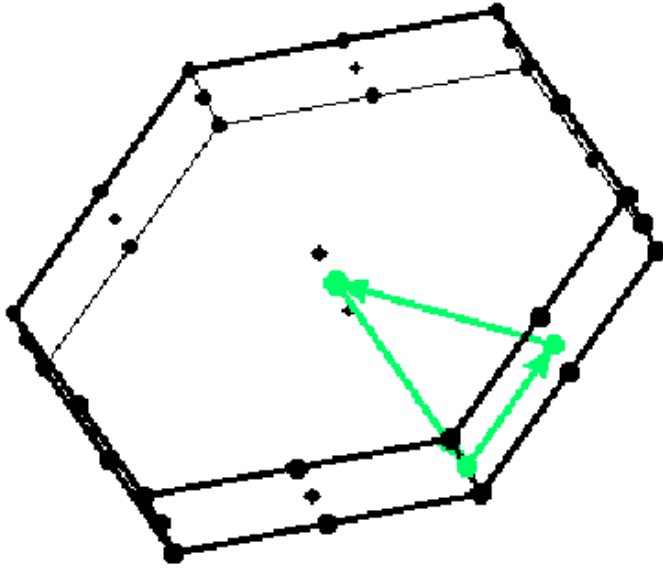


Figure 28: K-Path Selection

We also use the bands.x package to carry out band-related calculations and finally obtain the points for the band structure, which we plot in Excel.

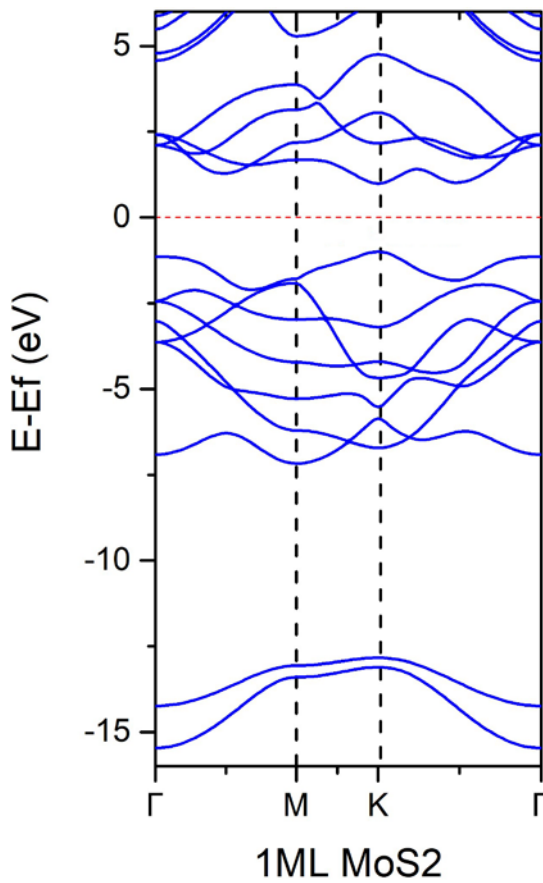


Figure 29: Band structure of pristine monolayer MoS<sub>2</sub>

We proceed to perform calculate density of states at different energy levels using dos.x package of Quantum Espresso. The value of gaussian spreading for brillouin-zone (degauss value) is kept at 0.01Ry.

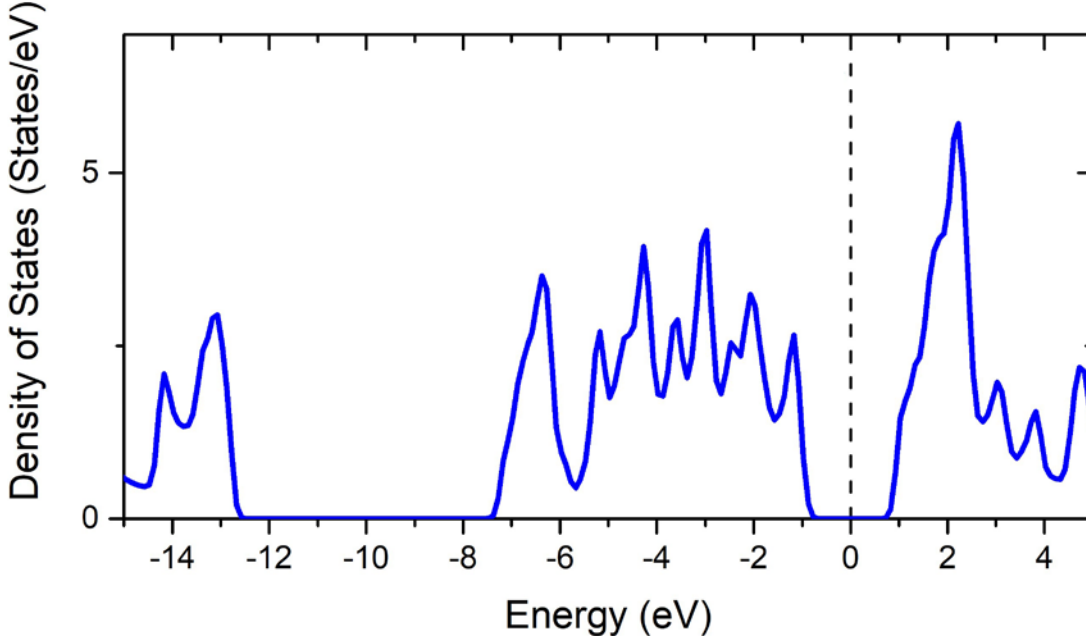


Figure 30: Density of states for pristine monolayer MoS<sub>2</sub> unit cell

We proceed to perform calculate projected density of states at different energy levels using projwfc.x package of Quantum Espresso. The value of gaussian spreading for brillouin-zone (degauss value) is kept at 0.01Ry. The PDOS of d orbital of Mo and p orbital of S plotted against their sum.

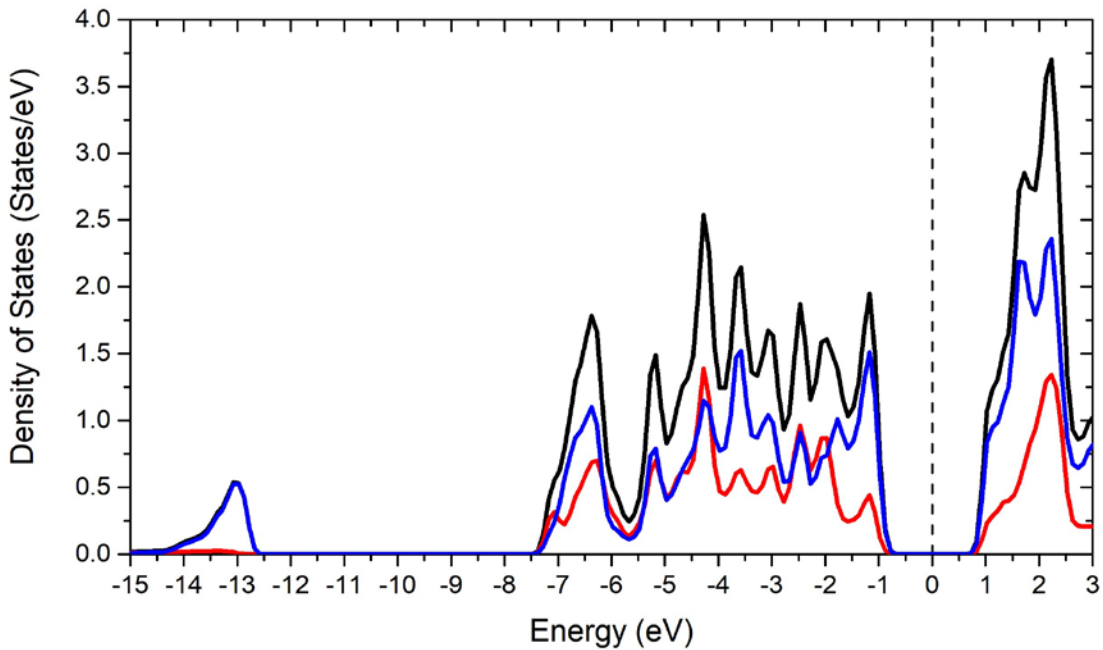


Figure 31: Projected Density of states for monolayer MoS<sub>2</sub> unit cell

The total Lowdin charges are calculated during the projected density of states calculation and comes up to 16.9563 e. In the PDOS plot, the blue line indicates the PDOS of 4d orbital of Mo atom, the red line indicates the PDOS of 3p orbital of S atom and black line indicates the sum of the two.

We proceed to perform simulations of scanning tunnelling microscope (STM) on the unit cell to examine the electron density distribution of the unit cell. The theoretical simulations of the STM current are based on the non-equilibrium Green function technique.

The bias voltage is kept at -1eV (0.0735Ry). The data for STM image is collected using the pp.x package of Quantum Espresso and saved to a Xcrysden structure file. Opening this file in Xcrysden, a top view projection of the 3D image is obtained. Then, the composite image of STM and molecular structure is constructed.

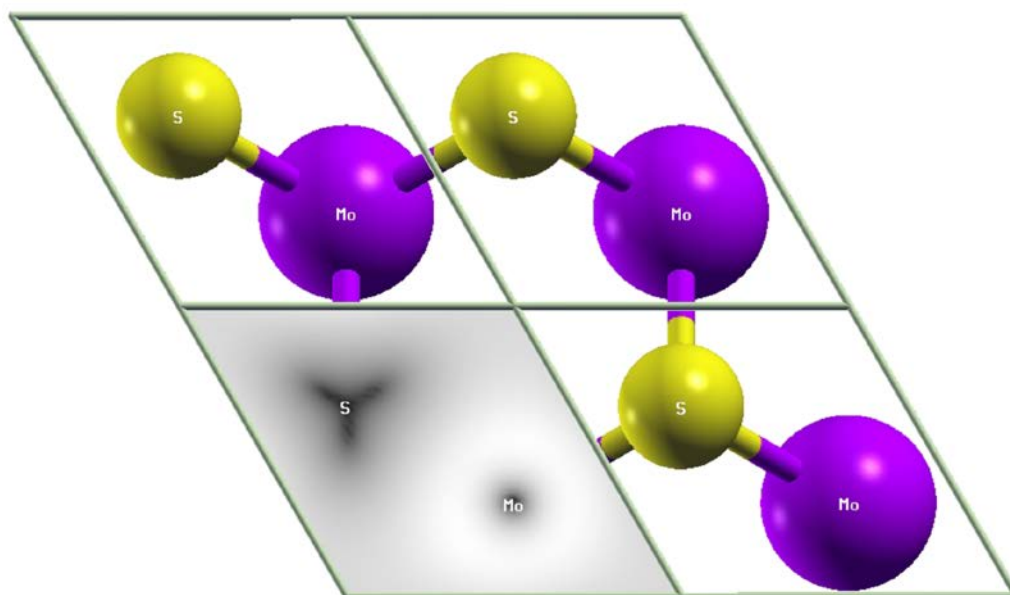


Figure 32: Simulated STM image of unit cell

Next, we create a 3x3 super-cell by simulating the unit cell SCF file in Xcrysden and changing the number of units drawn. The coordinates of all the atoms taken in angstroms from Atoms Info section. Then, the supercell is subjected to variable cell relaxation. After performing self-consistent field calculations, we obtain a band gap energy of 1.98eV, which is consistent with that of unit cell. The Fermi energy is calculated out to be -0.12eV, which is also consistent with that of unit cell.

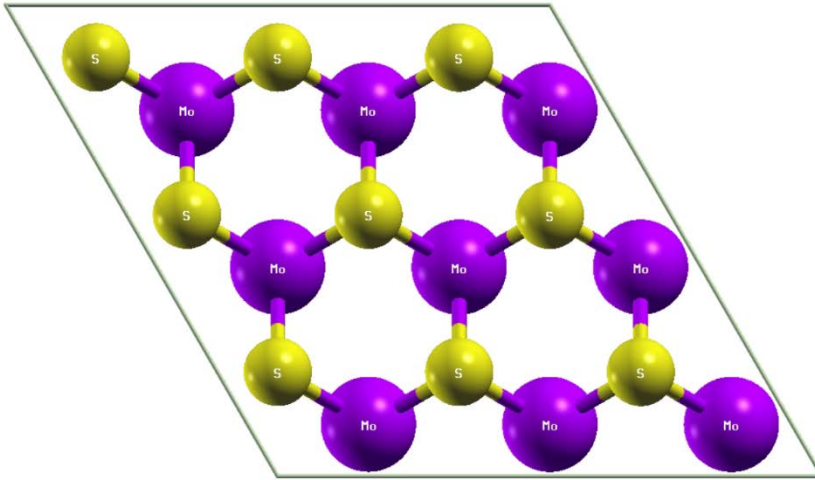


Figure 33: Top view of 3x3x1 MoS2 supercell, visualized in Xcrysden

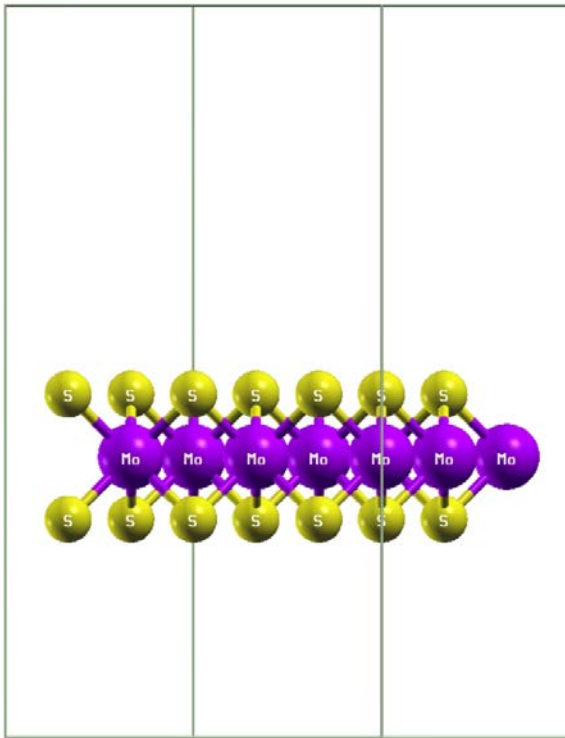


Figure 34: Side view of 3x3x1 MoS2 supercell, visualized in Xcrysden

Next, we perform a non self-consistent field calculations with a Monkhorst Pack grid of  $30 \times 30 \times 1$ . Then, we perform band calculations of the pristine super cell.



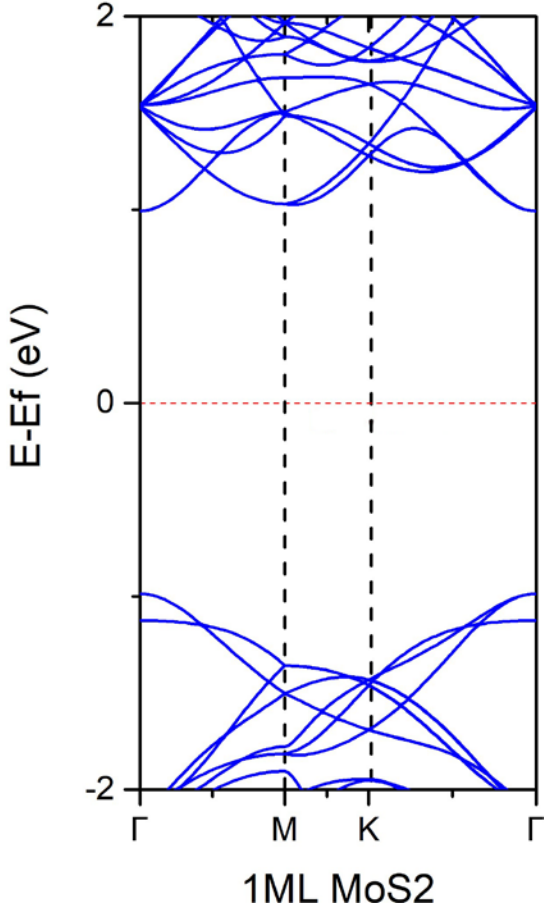


Figure 35: Band structure of 3x3x1 MoS2 supercell

The number of bands increased in the band structure as compared to unit cell. The presence of additional bands can be attributed to the folding of the Brillouin zone for the hexagonal lattice.

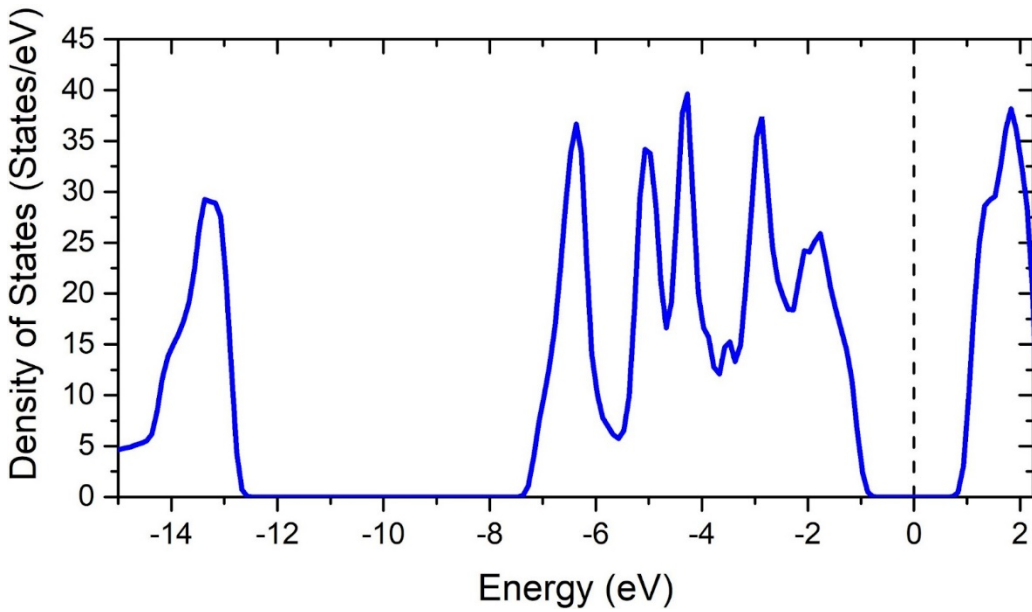


Figure 36: Density of states for pristine 3x3x1 super cell

A look into the DOS plot of supercell reveals a higher density of states due to the greater number of bands. The PDOS of Mo and S atom on the edge of super cell taken as the defect will be induced on the central Mo/S atoms. The PDOS of 4d orbital of Mo and 3p orbital of S plotted against their sum.

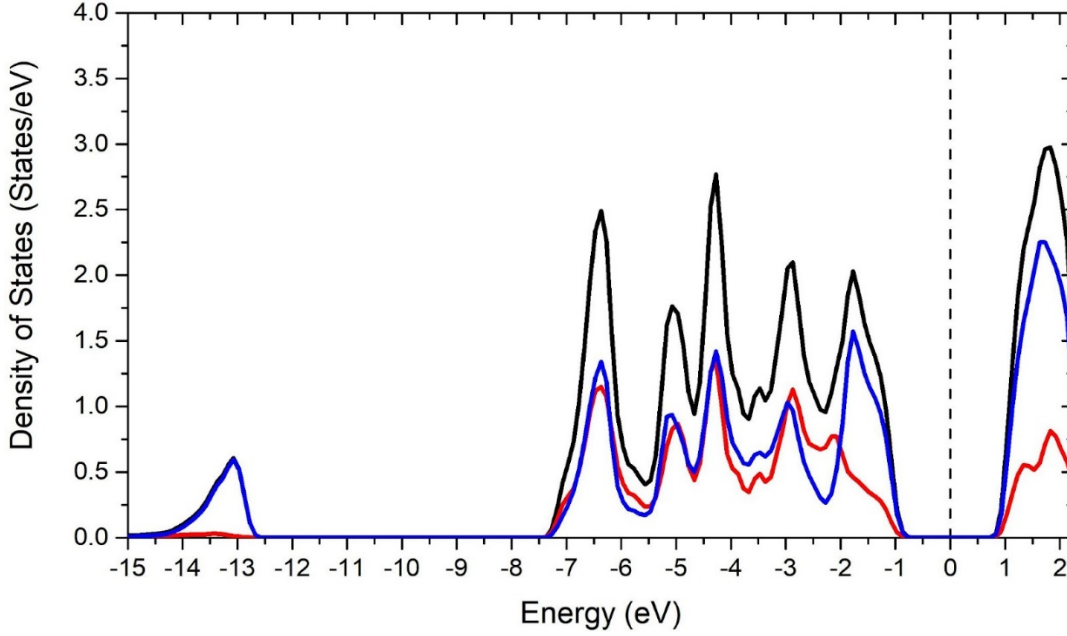


Figure 37: Projected Density of states for super cell

In the PDOS plot, the blue line indicates the PDOS of 4d orbital of Mo atom, the red line indicates the PDOS of 3p orbital of S atom and black line indicates the sum of the two.

We proceed to perform simulations of scanning tunnelling microscope (STM) on the super cell.

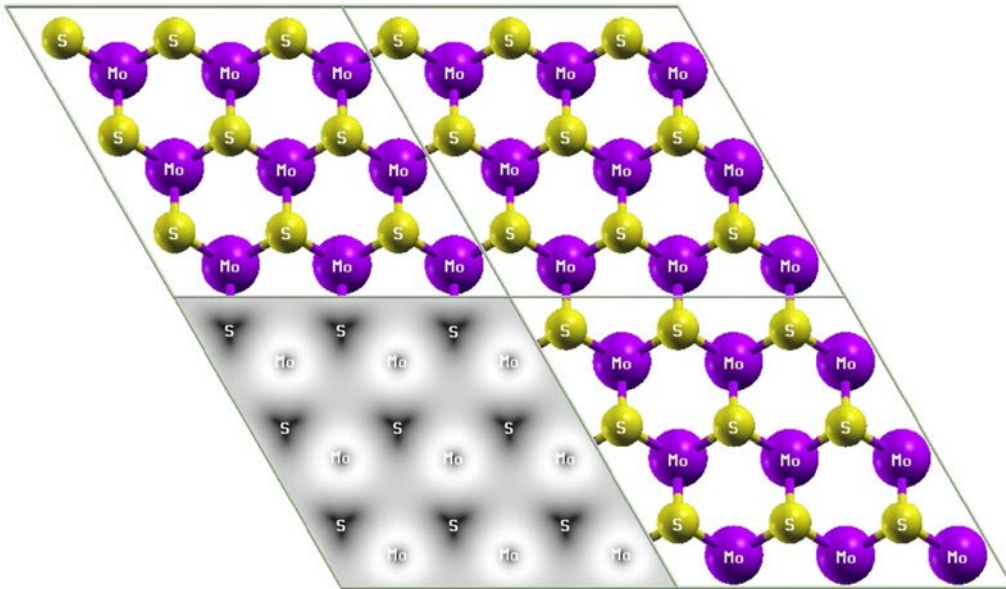


Figure 38: Simulated STM image of super cell

The STM image of supercell is consistent with that of a unit cell. The bias voltage is kept at -1eV (0.0735Ry).

Then, we attempt to induce the  $V_S$  defect. Atomic position of S atom attached to central Mo atom is noted down in super cell simulation. Then, we remove the S atom from the atomic position configuration in the SCF input files.

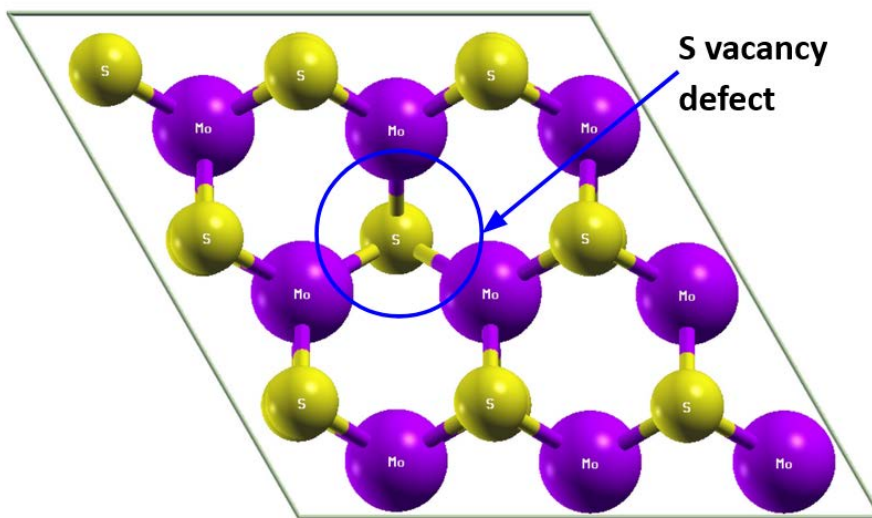


Figure 39: Top view of MoS<sub>2</sub> supercell molecular structure with  $V_S$  defect

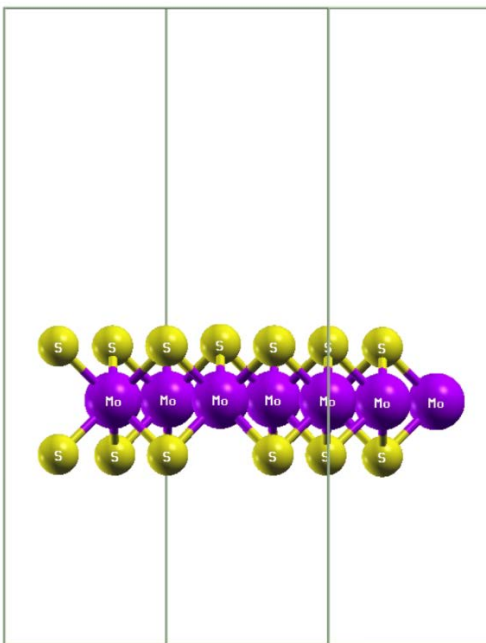


Figure 40: Side view of MoS<sub>2</sub> supercell molecular structure with  $V_S$  defect

Then, we implement the variable cell relaxation and obtain the final cell parameters and atomic positions of the 26 atoms present in the 3x3 super cell. After performing self-consistent field calculations, we obtain a band gap of 1.26 eV. After non self consistent field calculations, we perform band calculations.

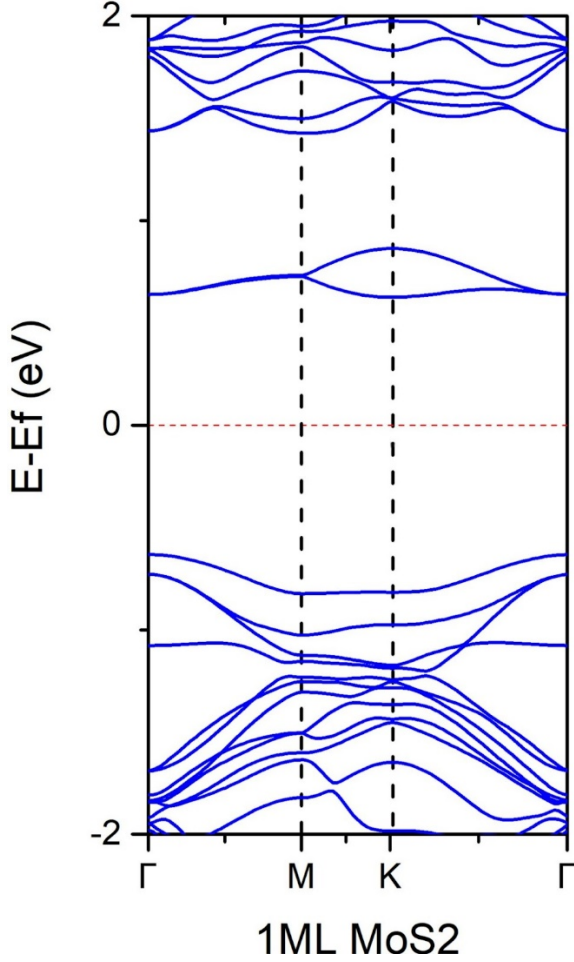


Figure 41: Band structure of MoS<sub>2</sub> with V<sub>s</sub> defect

The Fermi energy comes out to be -0.46eV. In the band structure, the zero is set to the Fermi level. We can observe that Mo atoms around V<sub>s</sub> responsible for states above the Fermi level and the states below Fermi level is due to V<sub>s</sub>.

We can also observe that introducing a sulphur defect resulted in a significant reduction in bandgap, a phenomenon which is corroborated by literature. [53]

Next, we proceed to plot the DOS and PDOS. PDOS of Mo and S atom on the edge of super cell is taken as S defect induced on central S atom. For Mo, we consider the 4d orbital and for S, the 3p orbital and plot the two against TDOS.

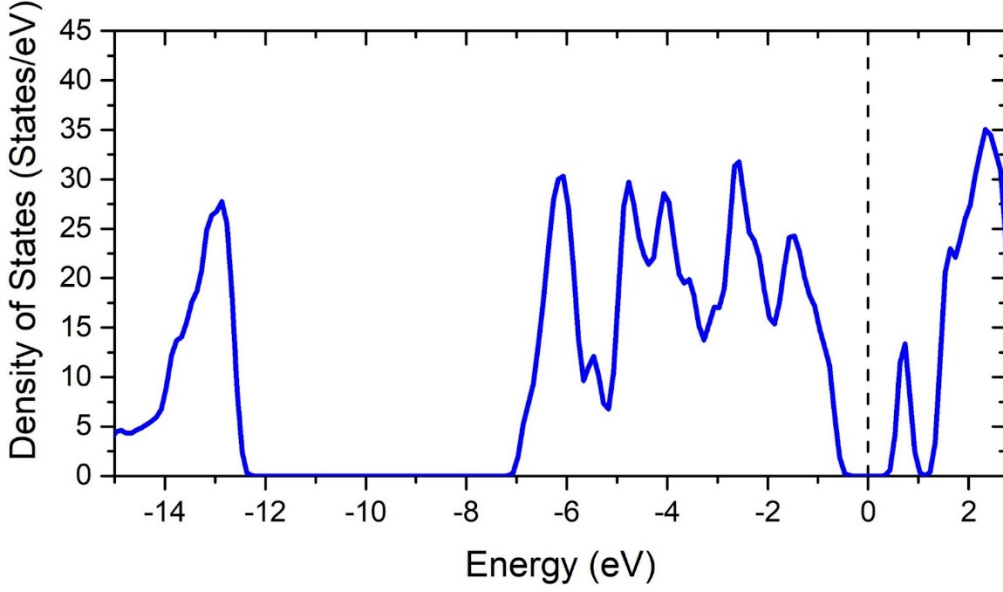


Figure 42: Density of states plot of MoS<sub>2</sub> with V<sub>s</sub> defect

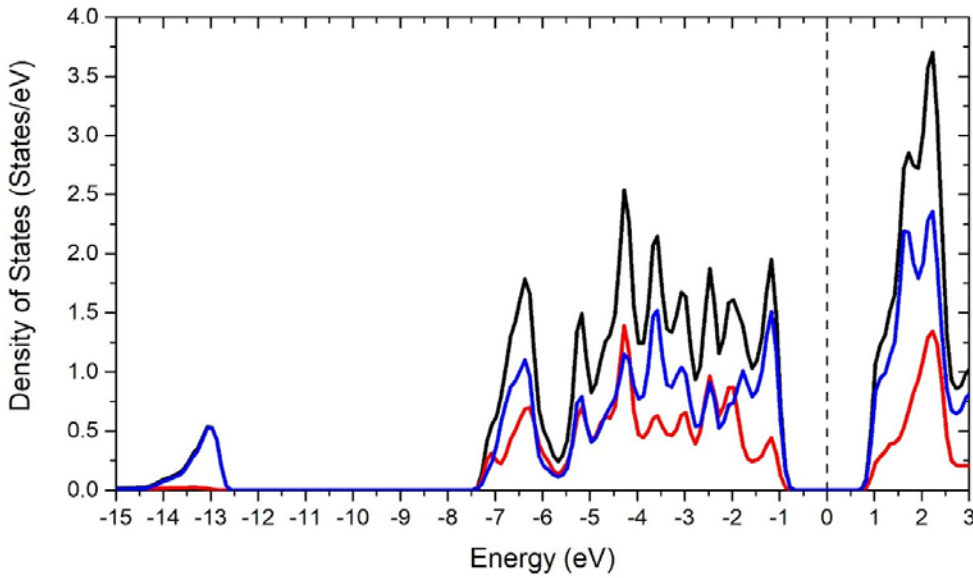


Figure 43: Projected Density of states plot of MoS<sub>2</sub> with V<sub>s</sub> defect

In the PDOS plot, the blue line indicates the PDOS of 4d orbital of Mo atom, the red line indicates the PDOS of 3p orbital of S atom and black line indicates the sum of the two.

The defect states to the right of the Fermi level are due to dangling bonds of Mo 4d orbitals caused by the unsaturated charges. To left of Fermi level, a shallow state change is observed due to reduced Mo 4d and S 3p orbital hybridization due to the S vacancy. The Sharp peak at  $E_f + 0.75\text{eV}$  level due to unbounded Mo orbitals. From the PDOS output file, we can observe that the change in Lowdin charge is  $-0.02e$ .

We proceed to perform STM simulations on the Vs molecular structure.

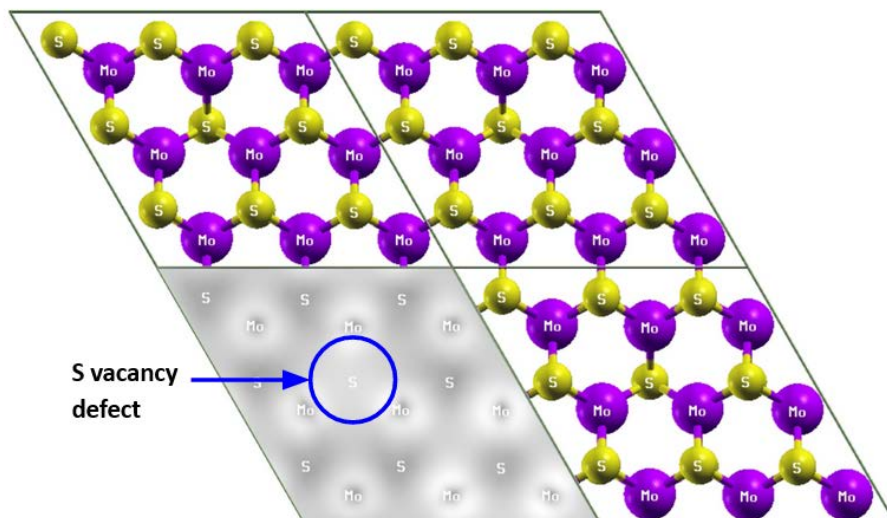


Figure 44: Simulated STM image of MoS2 with Vs defect

The STM image reproduces local charge variation at vicinity of S vacancy via the tiny contrast. Higher reactivity for this site can be deduced from reduction of bandgap and brighter appearance of dangling bonds in STM image. This is useful for facilitating molecular adsorption for 2D nanosensors.

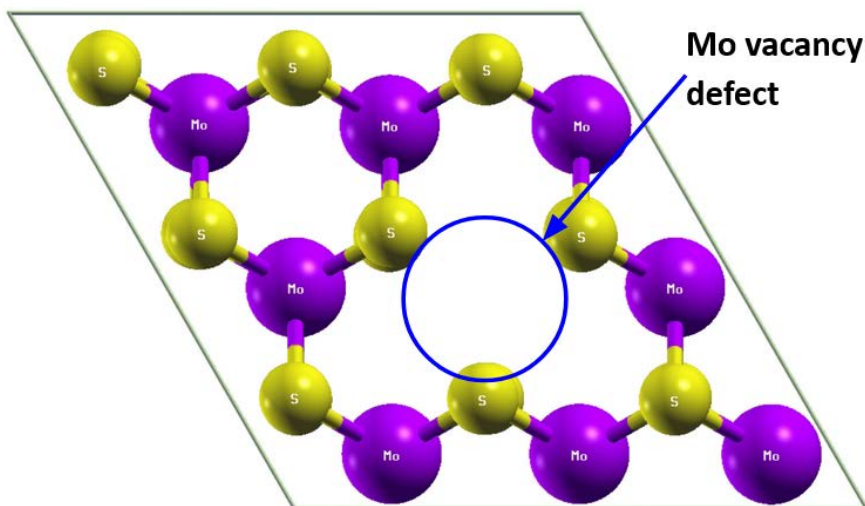


Figure 45: Top view of MoS2 supercell molecular structure with  $V_{Mo}$  defect

Then, we attempt to induce the  $V_{Mo}$  defect. Atomic position of central Mo atom is noted down in pristine super cell simulation. Then, we remove the Mo atom from the atomic position configuration in the SCF input files.



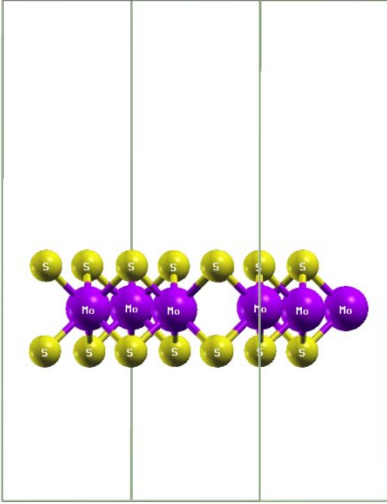


Figure 46: Side view of MoS<sub>2</sub> supercell molecular structure with V<sub>Mo</sub> defect

Next, we implement the variable cell relaxation and obtain the final cell parameters and atomic positions of the 26 atoms present in the 3x3 super cell. After performing self-consistent field calculations, we obtain a band gap of 0.9 eV. After non self consistent field calculations, we perform band calculations.

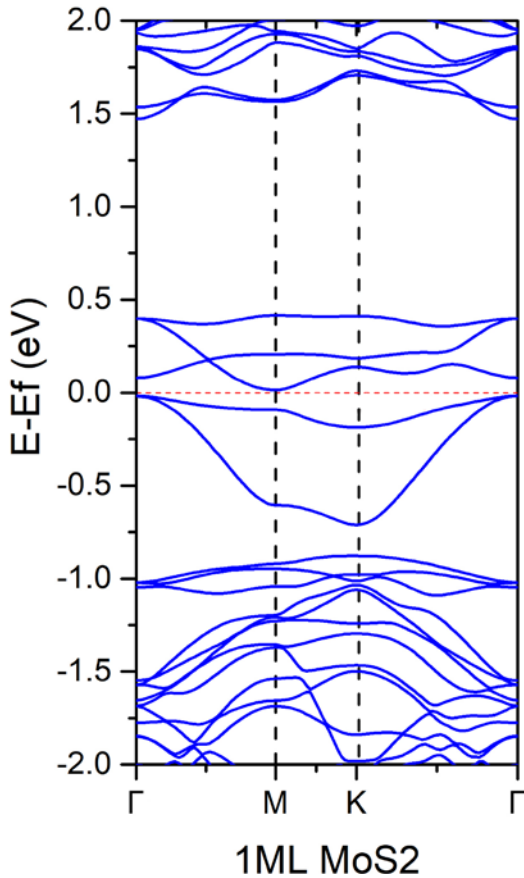


Figure 47: Band structure of MoS<sub>2</sub> with V<sub>Mo</sub> defect

The Fermi energy comes out to be  $-0.84\text{eV}$ . In the band structure, the zero is set to the Fermi level. We can observe that the midgap band splits into two bands centered around Fermi level.

Next, we proceed to plot the DOS and PDOS. PDOS of Mo and S atom on the edge of super cell is taken as Mo defect induced on central Mo atom. For Mo, we consider the 4d orbital and for S, the 3p orbital and plot the two against TDOS.

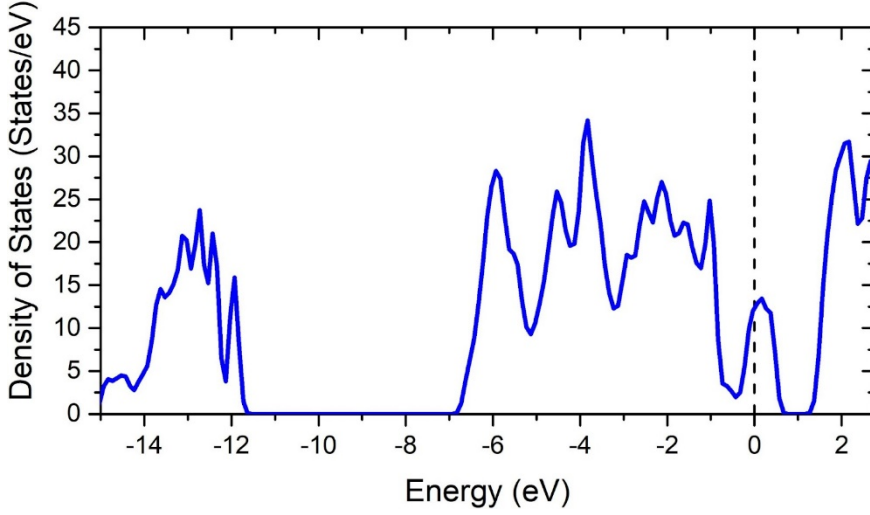


Figure 48: Density of states plot of MoS2 with  $V_{\text{Mo}}$  defect

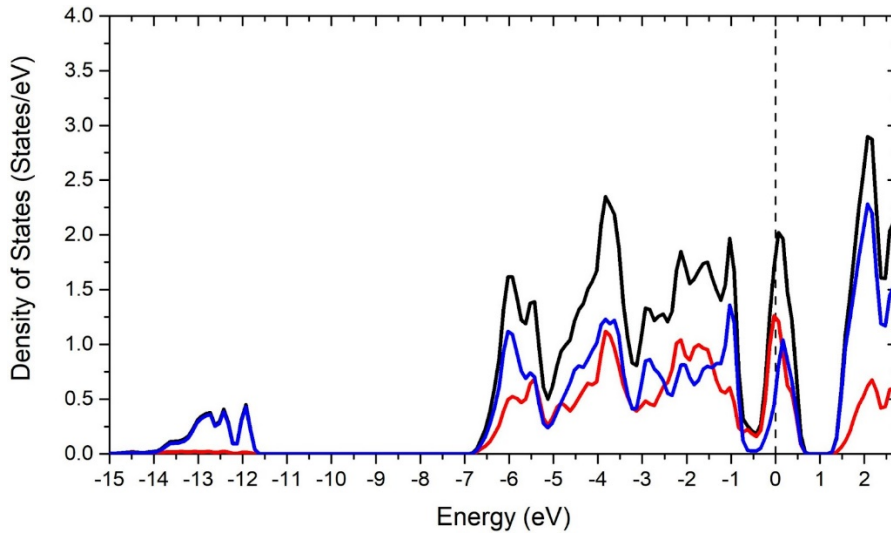


Figure 49: Density of states plot of MoS2 with  $V_{\text{Mo}}$  defect

In the PDOS plot, the blue line indicates the PDOS of 4d orbital of Mo atom, the red line indicates the PDOS of 3p orbital of S atom and black line indicates the sum of the two.



Defect states at the Fermi level arise from the dangling bonds of neighboring six S atoms, which are not saturated. From the PDOS output file, we can observe that the change in Lowdin charge is  $0.76e$ .

We proceed to perform STM simulations on the  $V_s$  molecular structure.

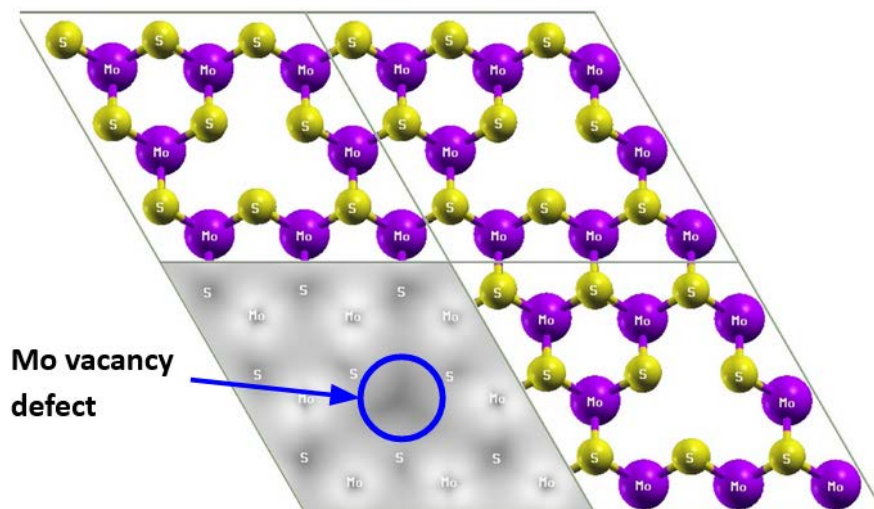


Figure 50: Simulated STM image of MoS<sub>2</sub> with  $V_{Mo}$  defect

The STM image reproduces local charge variation at vicinity of S vacancy via the tiny contrast. We can observe a small contraction of Mo network around the S vacancy, due to lower electronic density. Mo defects like these can be optimized to form S clusters. Unbounded orbitals due to the Mo defect are probably highly reactive to external adsorbates.

## 7. Summary & Future work

### 7.1 Summary

Starting off with an introduction to classification of materials based on dimensionality, we delved further into the world of two-dimensional materials. After studying the properties of 2D materials with respect to where electrical mechanical and optical characteristics, we examined the two types of synthesis techniques of 2D materials. Then we examine some important 2D material types such as graphene, TMDCs and xenos. In the next chapter, we delved deeper into molybdenum sulphide, a representative material for TMDCs and studied its various properties and electronic applications.

We examine the different types of defects present in 2D materials based on the dimensionality and further, examine the type of defects in  $\text{MoS}_2$  in detail. Further, we justify why studying point defects is necessary. The next chapter elucidates a brief history of computational studies and why we utilize computational methods in our report. The following chapter contains the results from the simulations run by us in Quantum Espresso.

### 7.2 Future Work

We can examine the effect of introducing multiple sulphur and molybdenum vacancies on the structural and electronic properties by examining the band structure, density of states, projected density of states and the STM image. Further, we can extend self-consistent field calculations to other types of defects such as substitutional defects, adatoms and Stone-Waller defects. Replacing Mo or S atom with atoms of other elements will yield different and interesting results, that can be extended for various applications, as studied by Hus et al. [49]

## 8. References

- [1] M. Tahir and U. Fatima, "Recent trends and emerging challenges in two-dimensional materials for energy harvesting and storage applications," *Energy Storage*, 2021.
- [2] V. V. Skorokhod and V. V. Pokropivny, "Classification of nanostructures by dimensionality and concept of surface forms engineering in nanomaterial science," *Materials Science and Engineering*, vol. 27, no. 5-8, pp. 990-993, 2007.
- [3] R. N. T. K. S. K. Jitendra N. Tiwari, "Zero-dimensional, one-dimensional, two-dimensional and three-dimensional nanostructured materials for advanced electrochemical energy devices," *Progress in Materials Science*, vol. 57, no. 4, pp. 724-803, 2012.
- [4] G. A. M. S. J. D. Z. Y. D. S. G. I. F. A. Novoselov KS, "Electric field effect in atomically thin carbon films," *Science*, vol. 306, no. 5696, pp. 666-669, 2004.
- [5] M. J. D. & Z. H. Chhowalla, "Two-dimensional semiconductors for transistors," *Nature Reviews Materials*, vol. 1, no. 16052, 2016.
- [6] N. G. M. S. P. e. a. Mounet, "Two-dimensional materials from high-throughput computational exfoliation of experimentally known compounds," *Nature Nanotech*, vol. 13, p. 246-252, 2018.
- [7] S. Lim, S. Kang, T. Yoo, S. Lee and H. Hwang, "Operation Mechanism of a MoS<sub>2</sub>/BP Heterojunction FET," *Nanomaterials*, vol. 8, no. 797, 2018.
- [8] W. Park, Y. Pak, H. Jang, J. Nam, T. Kim, S. Oh, S. Choi, Y. Kim and Cho, "Improvement of the Bias Stress Stability in 2D MoS<sub>2</sub> and WS<sub>2</sub> Transistors with a TiO<sub>2</sub> Interfacial Layer," *Nanomaterials*, vol. 9, no. 1155, 2019.
- [9] B. Cho and Y. Kim, "Preparation and Properties of 2D Materials," *Nanomaterials*, vol. 10, no. 764, 2020.
- [10] J. Lee, C. Park, T. Kim, Y. Kim and E. Kim, "K. Characteristics of P-type Conduction in P-doped MoS<sub>2</sub> by Phosphorous Pentoxide during Chemical Vapor Deposition," *Nanomaterials*, vol. 9, no. 1278, 2019.

- [11] W. Park, H. Jang, J. Nam, J. Kwon, B. Cho and Y. Kim, "Artificial 2D van der Waals Synapse Devices via Interfacial Engineering for Neuromorphic Systems," *Nanomaterials*, vol. 10, no. 88, 2020.
- [12] C. Ko, "Reconfigurable Local Photoluminescence of Atomically-thin Semiconductors Via Ferroelectric-assisted Effects," *Nanomaterials*, vol. 9, no. 1620, 2019.
- [13] S. Liang, M. Hasan and J. Seo, "Direct Observation of Raman Spectra in Black Phosphorus under Uniaxial Strain Conditions," *Nanomaterials*, vol. 9, no. 566, 2019.
- [14] R. Zhang and R. Cheung, "Mechanical Properties and Applications of Two-Dimensional Materials," in *Two-dimensional Materials - Synthesis, Characterization and Potential Applications*, InTech, 2016.
- [15] S. Z. Yi M, "A review on mechanical exfoliation for the scalable production of graphene," *J Mater Chem*, vol. 3, no. 22, pp. 11700-11715, 2015.
- [16] Y. H-D, "Chemical routes to top-down nanofabrication," *Chem Soc Rev*, vol. 42, no. 14, pp. 6006-6018, 2013.
- [17] H. J-K, "Large-area synthesis of highly crystalline WSe<sub>2</sub> monolayers and device applications," *ACS Nano*, vol. 8, no. 1, pp. 923-930, 2014.
- [18] G. A. M. S. Novoselov KS, "Two-dimensional gas of massless Dirac fermions in graphene," *Nature*, vol. 438, pp. 197-200, 2005.
- [19] D. W. a. K. M. I. a. L. A. I. Boukhvalov, "Hydrogen on graphene: Electronic structure, total energy, structural distortions and magnetism from first-principles calculations," *Phys. Rev. B*, vol. 77, no. 3, 2008.
- [20] W. Bao, X. Cai, D. Kim, K. Sridhara and M. Fuhrer, "High Mobility Ambipolar MoS<sub>2</sub> Field-Effect Transistors: Substrate and Dielectric Effects," *Appl. Phys. Lett*, vol. 102, no. 042104, 2013.
- [21] L. C, "Measurement of the elastic properties and intrinsic strength of monolayer graphene," *Science*, vol. 321, no. 5887, pp. 385-388, 2008.

- [22] L. Z. H. W. a. X. L. Zixin Xiong, “Structural Defects, Mechanical Behaviors, and Properties of Two-Dimensional Materials,” *Materials (Basel)*, vol. 14, no. 5, 2021.
- [23] D. J. F. S. T. J. B. V. V. K. S. V. M. A. K. G. K. S. Novoselov, “Two-dimensional atomic crystals,” in *Proceedings of the National Academy of Sciences*, 2005.
- [24] J. A. R. Eric M. Vogel, “Two-dimensional layered transition-metal dichalcogenides for versatile properties and applications,” *MRS Bulletin*, vol. 40, no. 7, pp. 558-563, 2015.
- [25] C. W, “Recent development of two-dimensional transition metal dichalcogenides and their applications,” *Mater Today*, vol. 20, no. 3, pp. 116-130, 2017.
- [26] B. Feng, Z. Ding, S. Meng, Y. Yao, X. He, P. Cheng, L. Chen and K. Wu, “ K. Evidence of silicene in honeycomb structures of silicon on Ag(111),” *Nano Lett.* , vol. 12, p. 3507–3511, 2012.
- [27] E. M, “Fundamentals and functionalities of silicene, germanene, and stanene,” *Riv Nuovo Cimento*, vol. 41, pp. 175-224, 2018.
- [28] F. T. E. a. R. M. Roberts, “Molybdenum disulfide of high surface area,” *J. Phys. Chem.*, vol. 63, 1959.
- [29] S. V. L. L. M. T. H. M. Jariwala D, “Emerging Device Applications for Semiconducting Two-Dimensional Transition Metal Dichalcogenides,” *ACS Nano*, vol. 8, no. 2, p. 1102–1120, 2014.
- [30] H. Z. Xiao Li, “Two-dimensional MoS<sub>2</sub>: Properties, preparation, and applications,” *Journal of Materiomics*, vol. 1, no. 1, pp. 33-44, 2015.
- [31] Y. H. V. D. F. T. C. M. C. M. Eda G, “Photoluminescence from chemically exfoliated MoS<sub>2</sub>,” *Nano Lett*, vol. 11, pp. 5111-5116, 2011.
- [32] S. M. K. N. K. O. P. F. A. G. G. M. S. P. N. Thomas, “2D MoS<sub>2</sub>: structure, mechanisms, and photocatalytic applications,” *Materials Today Sustainability*, vol. 13, 2021.
- [33] P. N. H. J. Akinwande D, “Two-dimensional flexible nanoelectronics,” *Nat Commun.*, vol. 5, no. 5678, 2014.

- [34] S. Z. M. D. B. A. E. M. Omnia Samy, "A Review on MoS<sub>2</sub> Properties, Synthesis, Sensing Applications," *Crystals*, vol. 11, no. 4, p. 355, 2021.
- [35] R. A. B. J. G. V. K. A. Radisavljevic B, "Single-layer MoS<sub>2</sub> transistors," *Nat Nanotechnol* , vol. 6, no. 147, p. e50., 2011.
- [36] L. H. L. H. J. L. S. Y. S. Y. Yin Z, "Single-layer MoS<sub>2</sub> phototransistors," *ACS Nano*, vol. 6, pp. 74-80, 2012.
- [37] Y. Liu, J. Peng, S. Wang, M. Xu, M. Gao, T. Xia, J. Weng, A. Xu and S. Liu, "Molybdenum Disulfide/Graphene Oxide Nanocomposites Show Favorable Lung Targeting and Enhanced Drug Loading/Tumor-Killing Efficacy with Improved Biocompatibility," *NPG Asia Mater*, vol. 10, 2018.
- [38] X. Ding, F. Peng, J. Zhou, W. Gong, G. Slaven, K. Loh, C. Lim and D. Leong, "Defect Engineered Bioactive Transition Metals Dichalcogenides Quantum Dots," *Nat. Commun.*, vol. 10, no. 41, 2019.
- [39] S. Catalán-Gómez, M. Briones, S. Cortijo-Campos, T. García-Mendiola, A. de Andrés, S. Garg, P. Kung, E. Lorenzo and J. Pau, "Breast Cancer Biomarker Detection through the Photoluminescence of Epitaxial Monolayer MoS<sub>2</sub> Flakes," *Scientific Reports*, vol. 10, no. 16039, 2020.
- [40] C. Choi, J. Leem, M. Kim, A. Taqieddin, C. Cho, K. Cho, G. Lee, H. Seung, H. Bae and Y. Song, "Curved Neuromorphic Image Sensor Array Using a MoS<sub>2</sub>-Organic Heterostructure Inspired by the Human Visual Recognition System," *Nat. Commun.* , vol. 11, no. 5934, 2020.
- [41] S. Sanjay, K. Sahoo and N. Bhat, "Alcohol-Based Sulfur Treatment for Improved Performance and Yield in Local Back-Gated and Channel-Length-Scaled MoS<sub>2</sub> FETs," *IEEE Trans. Electron Devices*, vol. 67, p. 3711–3715, 2020.
- [42] M. Dey, M. Dey, S. Alam, N. Das, M. Martin and N. Amin, "Study of Molybdenum Sulphide as a Novel Buffer Layer for CZTS Solar Cells," in *3rd International Conference on Electrical Engineering and Information Communication Technology*, Dhaka, 2016.

- [43] H. Xu, L. Xin, L. Liu, D. Pang, Y. Jiao, R. Cong and W. Yu, “W. Large Area MoS<sub>2</sub>/Si Heterojunction-Based Solar Cell through Sol-Gel Method,” *Mater. Lett.* , vol. 238, p. 13–16, 2019.
- [44] Y. Huang, Y. Wang, X. Zhang, F. Lai, Y. Sun, Q. Li and H. Wang, “N-Doped Carbon@nanoplate-Assembled MoS<sub>2</sub> Hierarchical Microspheres as Anode Material for Lithium-Ion Batteries,” *Mater. Lett.* , vol. 243, p. 84–87, 2019.
- [45] Z. a. N. Z. Wu, “Spectroscopic investigation of defects in two-dimensional materials,” *Nanophotonics*, vol. 7, no. 7, 2016.
- [46] C. K. R. E. M. D. R. M. F. C. A. Z. Jannik C. Meyer, “Direct Imaging of Lattice Atoms and Topological Defects in Graphene Membranes,” *Nano Letters*, vol. 8, no. 11, pp. 3582-3586, 2008.
- [47] N. Z. Y. T. S. Z. You YM, “Edge chirality determination of graphene by Raman spectroscopy,” *Appl Phys Lett* , vol. 93, no. 3112, 2008.
- [48] X. Z. S. N. Z. L. Y. S. J. K. J. L. P. M. A. B. I. Y. a. J.-C. I. Wu Zhou, “Intrinsic Structural Defects in Monolayer Molybdenum Disulfide,” *Nano Lett.* , vol. 13, no. 6, p. 2615–2622, 2013.
- [49] S. G. R. C. P. e. a. Hus, “Observation of single-defect memristor in an MoS<sub>2</sub> atomic sheet,” *Nat. Nanotechnol.* , vol. 16, pp. 58-62, 2021.
- [50] C. J. J. Y. Z. Z. Jinhua Hong, “Atomic Defects in Two-Dimensional Materials: From Single-Atom Spectroscopy to Functionalities in Opto-/Electronics, Nanomagnetism, and Catalysis,” *Advanced Materials*, vol. 29, no. 14, 2017.
- [51] M. C. Wei Hu, “Advances in Density Functional Theory and Beyond for Computational Chemistry,” *Front Chem*, vol. 9, 2021.
- [52] P. a. S. P. V. Lloyd, “Multiple Scattering Theory in Condensed Materials,” *Adv. Phys.* , vol. 21, p. 69–142, 1972.
- [53] L. T. Z. X.-D. Yang Ke, “Bandgap Engineering and Near-Infrared-II Optical Properties of Monolayer MoS<sub>2</sub>: A First-Principle Study,” *Frontiers in Chemistry*, vol. 9, p. 433, 2021.

- [54] Z. W. a. Z. Ni, “Spectroscopic investigation of defects in two dimensional materials,” *Nanophotonics*, vol. 151, 2016.